# Chapter 4

# Synthesis and Fabrication of Adsorbents for the Removal of Fluoride from Aqueous Solutions

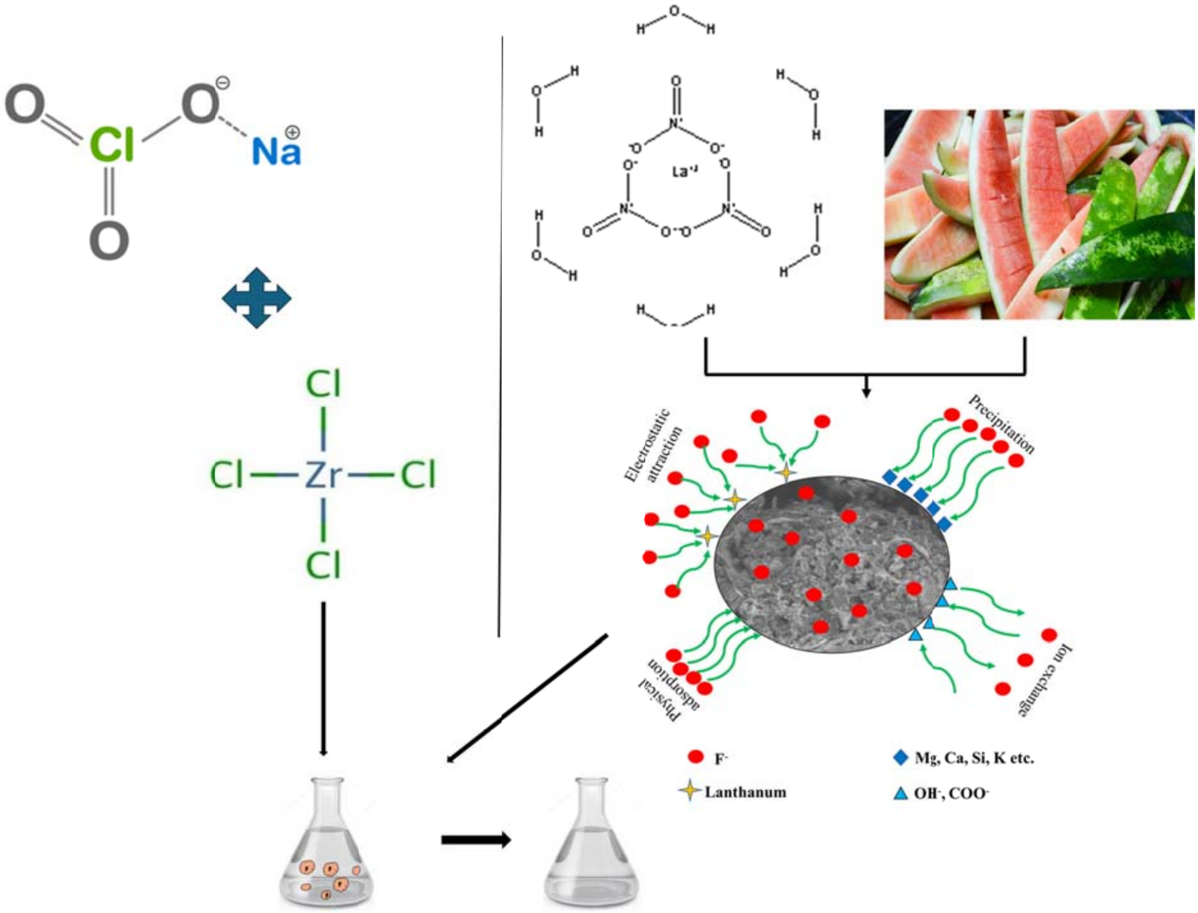

## 4.1. Introduction

One of the major concerns worldwide is fluoride contamination of water resources via natural and anthropogenic activities. Fluoride ingestion, however, has both positive (below 1.5mg/L) and negative (above 1.5mg/L) consequences. It lowers the risk of dental caries, but it can also cause tooth enamel and skeletal fluorosis after high exposure. Elevated levels of fluoride in groundwater reservoirs are reported worldwide, including the United States, South Asia, the Middle East, and Africa (Podgorski and Berg, 2022). Therefore, creating effective and dependable methods to eliminate excessive fluoride from the water environment is crucial. Fluoride can now be eliminated from water and wastewater using methods including coagulation, electrochemical processes, membrane filtering, and ion exchange columns. However, these technologies have shortcomings and cannot be used in many parts of the world, particularly in developing and underdeveloped nations, because of their high costs and numerous drawbacks such as high energy consumption, pH dependence, high installation and maintenance costs, membrane fouling, scaling, etc. (Savari et al., 2023). Adsorption technology has been exhaustively investigated and offers a very effective, simple, and affordable method for remediating fluoride from water, among other generally used treatment technologies (He et al., 2020). Certain adsorbents, like metal-impregnated biochar and zirconium-based adsorbents, are getting prominence as environmentally friendly, temperature-effective, sustainable, and affordable adsorbents (Yan et al., 2022).

Not much studies have been done on the watermelon biomaterial to remove contaminants like fluoride (Lingamdinne et al., 2022; Muhammad et al., 2020; Sadhu et al., 2021). Biochar produced by carbonizing watermelon rind was used as an adsorbent, but watermelon rind biochar had less adsorption capacity as a result, more modification techniques should be applied to increase the adsorption capability at neutral pH levels. Rare earth metals such as lanthanum and zirconium have a strong affinity for fluoride, based on previous investigations (Gan et al., 2019; Habibi et al., 2019; Singh et al., 2020; Yan et al., 2022). Many characteristics of lanthanum, such as its high electron affinity relative to other rare earth metals, stability at high temperatures, and extremely low solubility in water, make it an excellent adsorbent (Yin et al., 2022). large adsorption capacities have been reported for Zirconium-based adsorbents with chemical and thermally stability in fluoride-containing effluents (Sonal and Mishra, 2021). **Figures 4.1 and 4.2** illustrate a brief review of lanthanum and zirconium-based adsorbents respectively, including their characteristics, preparation process, and main applications. Therefore, impregnating metals such as lanthanum or zirconium may be a practical way to save costs while increasing the adsorption capacity of adsorbents.

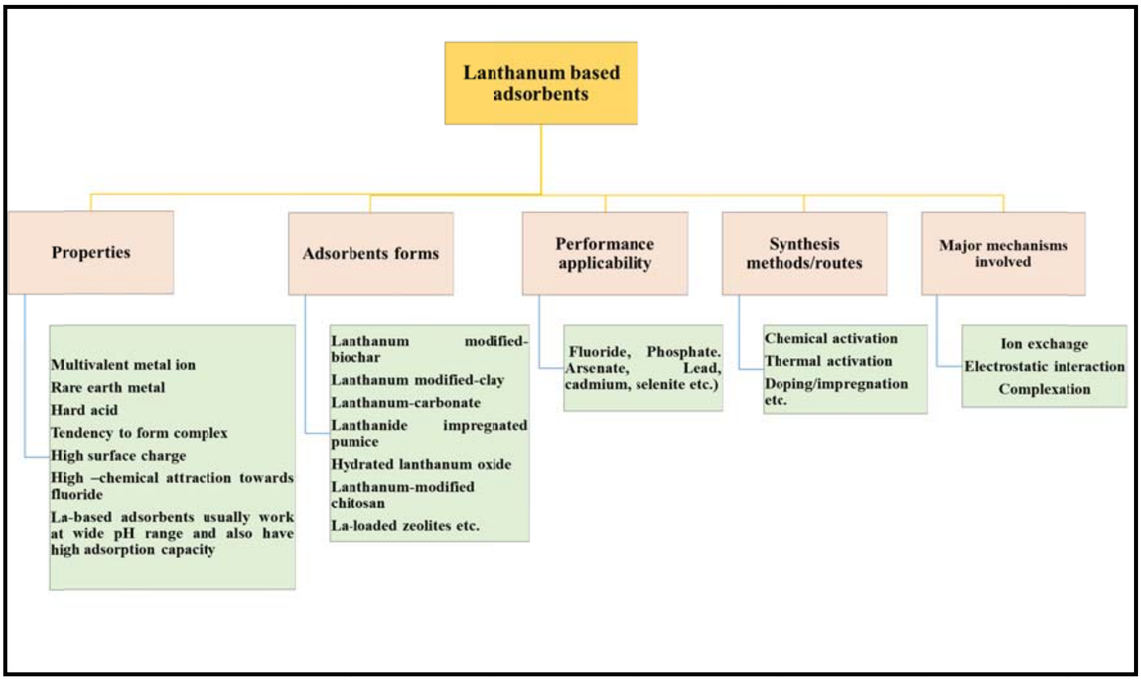

**Fig.4.1.** Lanthanum-based adsorbents

A new class of three-dimensional crystalline organic-inorganic porous hybrid materials called metal-organic framework (MOF) have emerged in addition to metal-impregnated biochar as promising candidates for a variety of applications, such as catalysis, ion exchange, sensors, as well as the adsorption and removal of hazardous materials (Sonal and Mishra, 2021; Yang et al., 2019).

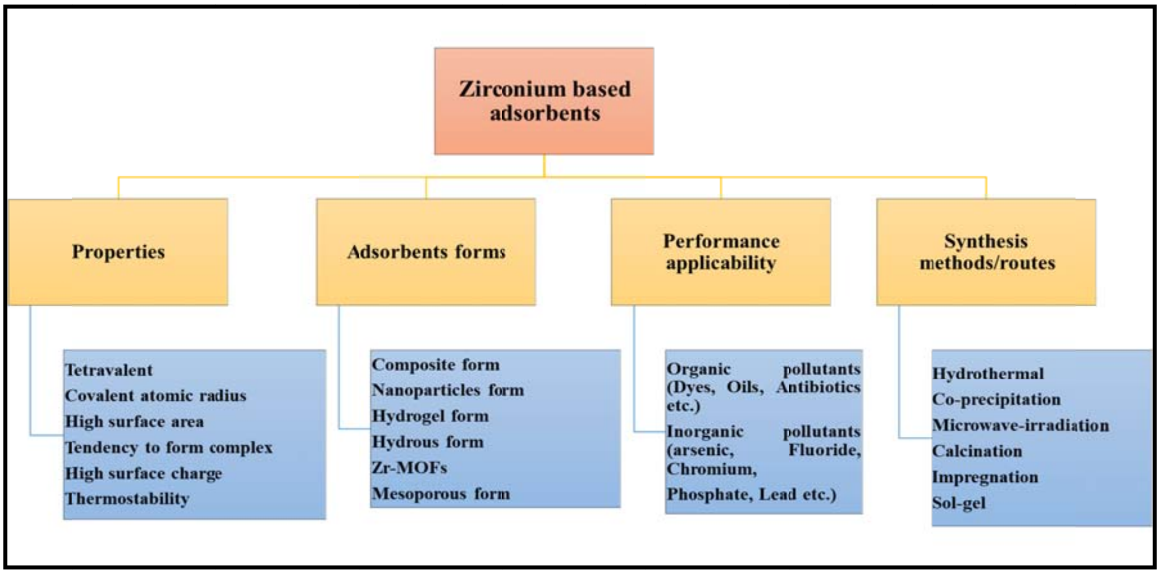

**Fig.4.2.** Zirconium-based adsorbents

Bile salt sodium cholate is an amphiphilic molecule that aggregates in aqueous solutions to help in the absorption and transfer of fat-soluble vitamins, lipids, and cholesterol. Furthermore, the stiff helical superstructure produced from bile salts makes it suitable for the production of new materials that can be used as catalysts, chiral materials, biosensors, and adsorbents (Sadhu and P, 2023). This study examined the defluoridation capability of zirconium cholate (Zr-CH), which was created by combining sodium cholate, a bile salt, with zirconium chloride and has not been widely explored till date.

So, the key objectives of the research discussed in this chapter are (1) fabrication of lanthanum-impregnated watermelon biochar (3WMB-LN) from locally obtained watermelon rind for defluoridation. Adsorption kinetics and equilibrium have been determined. The various optimization parameters such as the impact of solution pH, adsorbent dosage, concentration of fluoride solution, contact time, and temperature have been investigated. 3WMB-LN was also applied on real water samples. Through the use of the Langmuir and Freundlich adsorption models, the performance of the biochar was evaluated. To better understand the adsorption mechanism, the thermodynamics, and kinetics of the process were also examined, and the adsorption capacity of 3WMB-LN was compared to the adsorbents for fluoride removal reported in literature.

(2) to synthesize Zirconium cholate (Zr-CH) adsorbent from zirconium oxychloride ($ZrOCl_2 \cdot 8H_2O$) and sodium cholate ($C_{24}H_{39}NaO_5$). Similar to 3WMB-LN, Zr-CH's equilibrium and adsorption kinetics have been determined. The adsorption parameters namely pH, adsorbent dosage, fluoride solution concentration, contact time, and temperature on the adsorption process were also examined and optimized. Additionally, the application of Zr-CH to actual water was assessed. The effectiveness of the Zr-CH was assessed using the Langmuir and Freundlich adsorption models. The thermodynamics and kinetics of the process were also investigated, and the adsorption capacity of Zr-CH was compared to previously reported adsorbents for fluoride removal.

## 4.2. Determination of fluoride content

The concentration of fluoride in the solution was determined using an ion-selective electrode both before and after the adsorption of fluoride by the adsorbents under study (Thermo Scientific ORION STAR A214). The equipment was calibrated by analyzing a fluoride solution with a known concentration and calculating the unknown fluoride concentration. A TISAB buffer [1:10 (TISAB: sample)] was used for the analysis.

## 4.3. Characterization of the materials

3WMB-LN and Zr-CH were characterized by FTIR, TGA, XRD, BET, SEM-EDS and XPS techniques. Details of the instruments are discussed in **section 2.3** in **Chapter 3** of the thesis.

## 4.4. Batch adsorption experiment

The adsorption potential and the process optimization of the adsorbents under study for fluoride removal from aqueous solution were studied through a batch adsorption method, which was carried out in 100 mL polypropylene conical flasks. The fluoride removal (%) was calculated using **Equation 3.1** of **Chapter 3**.

## 4.5. Adsorption parameters optimization

Various adsorption parameters such as pH, contact time, adsorbent dosage, concentration, temperature were varied and interference studies were carried out to find the optimum conditions for the study. Details of these parameters are mentioned in **section 3.3** of Chapter **3** of the thesis.

## 4.6. Isotherms and kinetics analysis for fluoride adsorption

Details of isotherm models and kinetics models are summarized in **Tables 3.1 and 3.2** of **Chapter 3** of this thesis respectively.

This chapter is divided into two subchapters. **Chapter 4A** describes the synthesis, preparation, and optimization of lanthanum-modified biochar from watermelon rind and its potential for remediation of fluoride from aqueous solution and **Chapter 4B** discusses the synthesis and optimization of Zr-CH from zirconium chloride and sodium cholate and its potential for remediation of fluoride from aqueous solution.

# Chapter 4A

## Preparation and Synthesis of Lanthanum Impregnated Biochar (WMB-LN) for the Removal of Fluoride from Aqueous Solution

### 4A.1. Materials and Methodology

**4A.1.1. Chemical and other materials:** Lanthanum Nitrate, conductivity water, watermelon rind, weighing balance, muffle furnace, hot air oven, glass wares, crucible with lid.

**4A.1.2. Preparation and Synthesis of Lanthanum-impregnated biochar:** The collection and preparation of WMR are described in section **3B.1.1. and 3B.1.2** of **Chapter 3B**. The methodologies used for the preparation and synthesis of lanthanum-impregnated biochar are depicted in the flow chart below (**Figure 4A.1).**

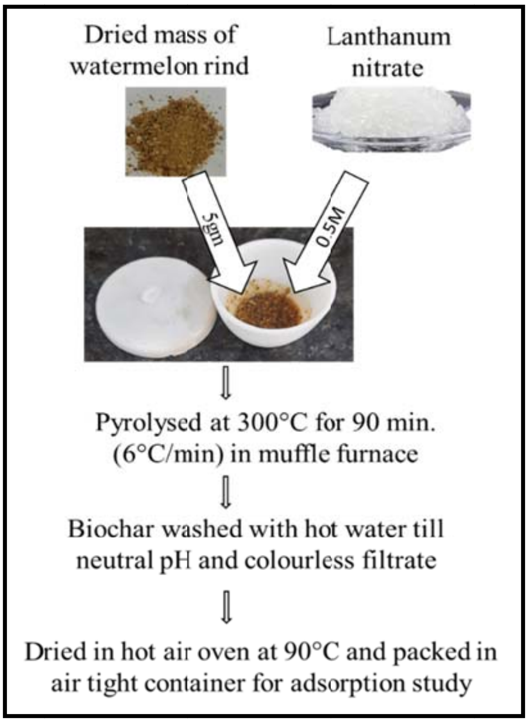

**Fig. 4A.1.** Synthesis of lanthanum-impregnated biochar

For the synthesis of lanthanum-impregnated biochar, to 10 mL solution of 0.5 M lanthanum nitrate, 5g of WMR powder was added and stirred to make a slurry. The slurry of WMR powder and lanthanum nitrate was Pyrolysed in a muffle furnace at 300 $^{o}$C (heating rate 10$^{o}$C/min) for 90 min. It was observed that in the presence of La, the biochar formation could occur at a lower temperature of 300$^{o}$C. The formed lanthanum-impregnated - biochar was thoroughly washed with hot water and dried at $100^0$C and the resultant product was 3WMB-LN was well characterized and used for further adsorption studies.

## 4A.2. Results and Discussion

**4A.2.1.Batch study:** For optimization of fluoride removal using 3WMB-LN, effect of several parameters such as pH, contact time, adsorbent dose, initial concentration of fluoride, temperature, and effect of coexisting anions was investigated.

**4A.2.2. Effect of solution pH on adsorption of fluoride:** The effect of pH on the removal of fluoride (25 mg/L) using 50mg 3WMB-LN was investigated by equilibration at room temperature for 3 hours in the pH range 2-10. 3WMB-LN exhibited effective removal (~ 91%) of fluoride in the pH range 2- 3 followed by a fast decline in adsorption efficiency **(Figure 4A.2)**. The protonation or deprotonation of some functional groups, such as amino and hydroxyl, and fluoride species are affected strongly by solution pH (Wang et al., 2018). The decline in fluoride adsorption efficiency for 3WMB-LN with increase in pH may be attributed to competition of $OH^-$ ions with fluoride ions for active adsorption sites on 3WMB-LN (Yu et al., 2015).

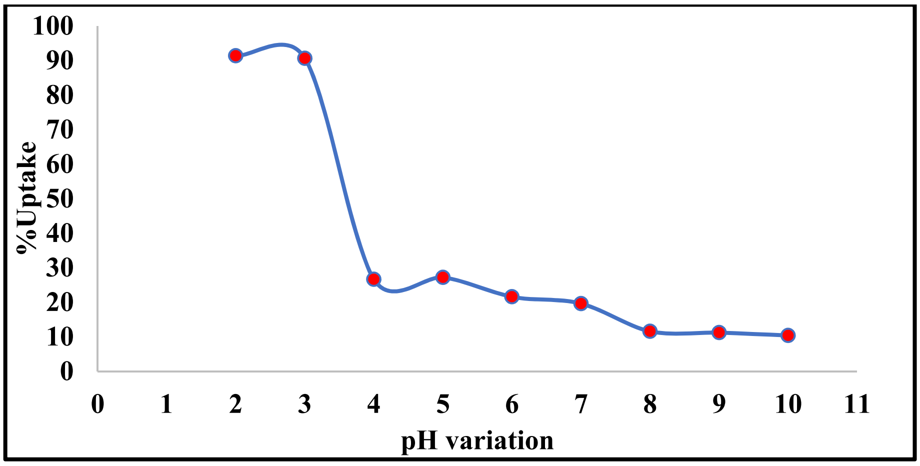

**Fig. 4A.2.** Effect of pH on removal of fluoride from 3WMB-LN (contact time: 3 h, dose: 0.05g, initial fluoride concentration: 25mg/L, volume:25mL).

**4A.2.3. Effect of dose on adsorption of fluoride:** The effect of 3WMB-LN dose on the efficiency of defluoridation of 25 mL of 25 mg/L fluoride-containing solution was investigated by equilibrating for 3 h with 0.01 - 0.1g of 3WMB-LN **(Figure 4A.3(a))** at pH **3**. It was found that amount of fluoride uptake increased with an increase in 3WMB-LN dose due to increased availability of active sites (Sadhu et al., 2021).

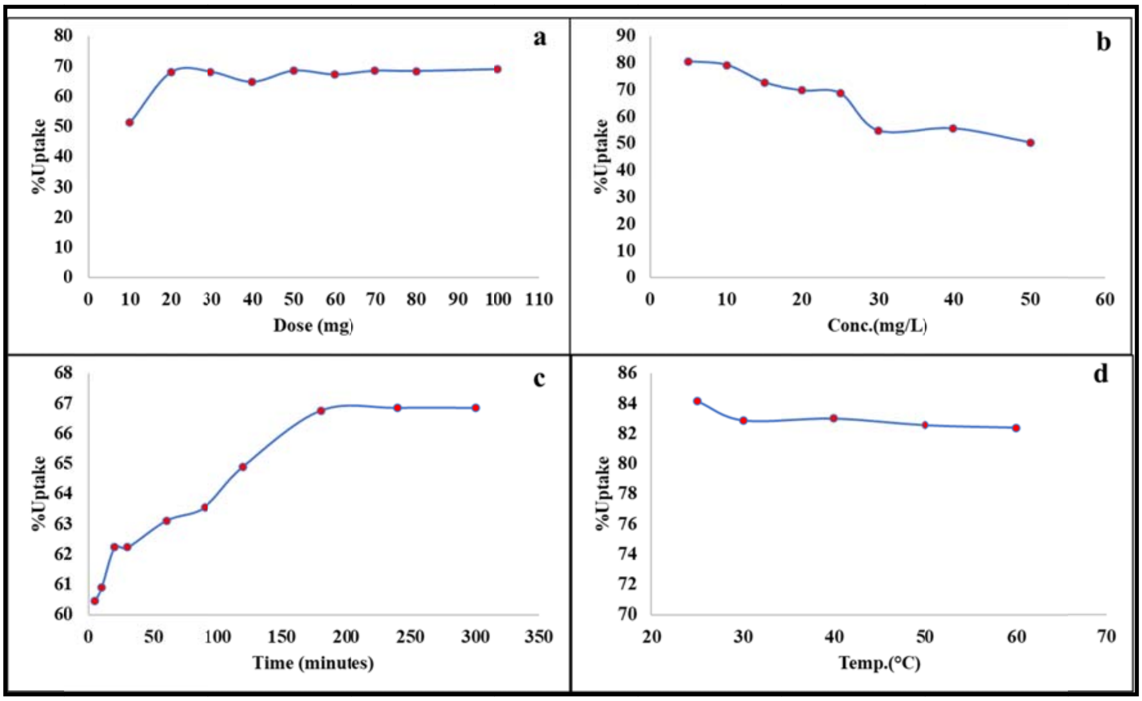

**Fig. 4A.3.** Effect of **(a)** adsorbent dose (pH: 3, contact time: 3 h, fluoride concentration: 25mg/L), **(b)** conc. variation (pH: 3, contact time: 3 h, dose: 0.02g, initial), **(c)** contact time (pH: 3, dose: 0.02g, and fluoride concentration: 25mg/L), and **(d)** temperature (pH: 3, contact time: 3 h, dose: 0.02g, fluoride concentration: 25mg/L) on % uptake of fluoride in aqueous solution.

**4A.2.4. Effect of Contact Time and Kinetics Study:** Experiments were conducted by equilibrating 25 mL of 25 mg/L fluoride solution at pH 3 with 0.02 g of 3WMB-LN for various time periods (5 to 300 minutes), to optimize the impact of contact time **(Figure 4A.3c).** The maximum uptake was observed and remained constant after 180 minutes of equilibration. A significant amount of fluoride (60%) was removed during the first five minutes, and the removal rate thereafter gradually increased until equilibrium was attained. The wide solute concentration gradient and the fact that all adsorbent sites were initially vacant may have contributed to the change in the rate of removal. Later, the rate of adsorption significantly decreased when both the number of adsorption sites and the fluoride concentration dropped (Ali et al., 2015).

For the kinetic study pseudo-first-order and pseudo-second-order models were explored **(Figure 4A.4 a and b).** The calculated rate constants and $R^2$ values for first and second-order reactions are shown in **Table 4A.1.** It was observed that compared to the pseudo-first-order experimental $q_e$ values of the pseudo-second-order equation were closer to the computed $q_e$

values of the pseudo-second-order. At 298 K, the regression coefficient ($R^2$) for the pseudo-second-order model was 0.9998, indicating the model to be the best kinetic fit with chemical interactions playing a major role in the uptake of fluoride (Khan et al., 2022).

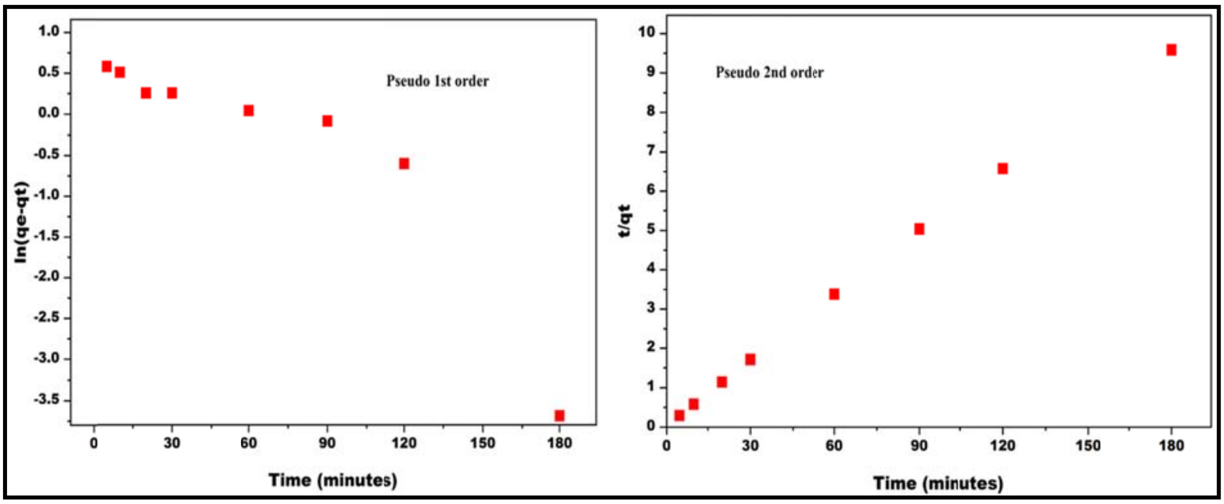

**Fig. 4A.4.** Kinetics models for fluoride adsorption using 3WMB-LN

**Table 4A.1** Kinetics parameters of Pseudo- first- order, Pseudo -second-order models for the adsorption of fluoride onto 3WMB-LN

| Kinetic models | Kinetic parameters | |
|---|---|---|
| **Pseudo 1st order** | **$K_1$(min$^{-1}$)** | -0.00011 |
| | **$q_e$ (mg/g)** | 2.65 |
| | **$R^2$** | 0.81 |
| **Pseudo 2nd order** | **$K_2$(gmg$^{-1}$ min$^{-1}$)** | 0.03 |
| | **$q_e$, cal (mg/g)** | 18.73 |
| | **$q_e$, exp(mg/g)** | 18.80 |
| | **$R^2$** | 1.00 |

**4A.2.5. Effect of initial concentration of fluoride and isotherm study for 3WMB-LN:** The concentration of fluoride was varied in the range 5 to 50 mg/L **(Figure 4A.3b)** while other factors such as pH (3), dose:(0.02g), volume (25 mL), and contact time (180 minutes) were kept constant. It was found that as fluoride concentration increased, fluoride uptake decreased because of lack of active sites (Kumar et al., 2019b).

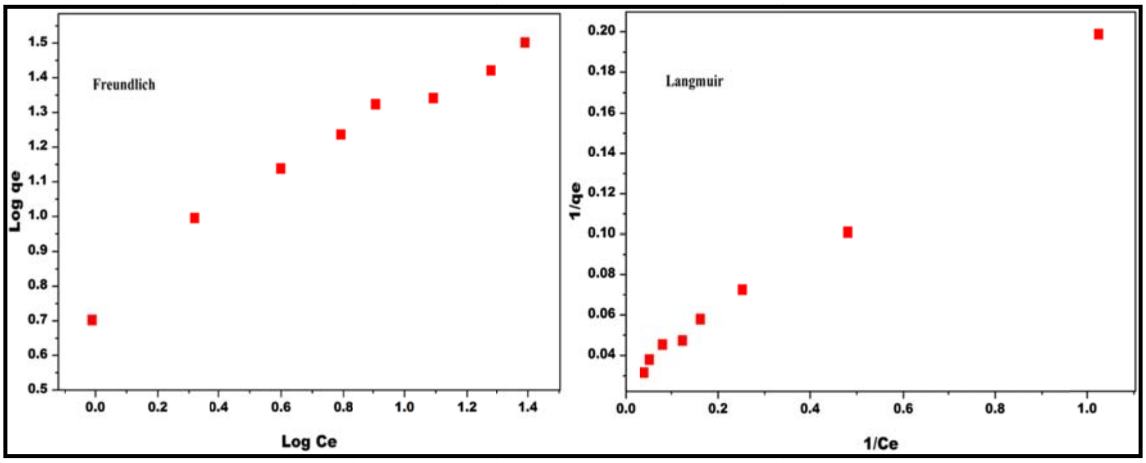

**Fig. 4A.5.** Isotherm models for uptake of fluoride using 3WMB-LN

Freundlich and Langmuir's isotherms were employed to understand the adsorption behavior of 3WMB-LN. **Table 4A.2 and Figure 4A.5** display the results of the same. The Langmuir model ($R^2$ = 0.996) offered a better fit to this study than the Freundlich model ($R^2$ = 0.966), demonstrating that primarily adsorption occurred on a homogenous surface (Zhou et al., 2019). The maximum fluoride adsorption capacity of 3WMB-LN was found to be 35.714mg/g. The comparison of the adsorption capacity of 3WMB-LN and the various adsorbents reported in the literature for fluoride has been summarized in **Table 4A.3**.

**Table 4A.2.** Isotherm parameters of Langmuir and Freundlich, for the adsorption of fluoride by 3WMB-LN.

| Isotherm models | Isotherm parameters | Numerical value |
|---|---|---|
| Freundlich isotherm | $K_f$ ($L.g^{-1}$) | 6.088 |
| | 1/n | 0.533 |
| | $R^2$ | 0.966 |
| Langmuir isotherm | $q_{max}$ (mg/g) | 35.714 |
| | $K_L$ (L. $mmol^{-1}$) | 0.170 |
| | $R^2$ | 0.996 |

**Table 4A.3**. Reported adsorbents and comparison for fluoride removal using biochar and Lanthanum based adsorbents

| Biochar | | | | | |
|---|---|---|---|---|---|
| **Sr. No.** | **Raw Materials and adsorbents name** | **Other parameters** | **pH** | **$Q_{max}$ (mg/g)** | **References** |
| 1 | Pinewood char (PB) | Conc.: 1-100mg/L, dose: 15g/L, time: 48h | 2 | 7.66 | (Mohan et al., 2012) |
| 2 | Pine bark char (PW) | | | 9.77 | |
| 3 | Corn stover biochar | Conc.: 1-100mg/L, | 2 | 6.42 | (Mohan et al., |

| | | | | | |
|---|---|---|---|---|---|
| | (CSBC) | dose: 5g/L, time: 72h | | | 2014) |
| 4 | Nanosized raw rice husk biochar (RRB) | Conc.: 3-10mg/L, dose: 1g/L, 1h | 7 | 21.7 | (Goswami and Kumar, 2018) |
| 5 | Bovine bone biochar (BBC) | Conc.: 5-35mg/L, dose: 2g/L, time: - | 8 | 5.05 | (Zhou et al., 2019) |
| 6 | Okra stem biochar (OSBC) | Conc.: 2-100mg/L, dose: 2.5g/L, time: 48h | 2 | 20 | (Kumar et al., 2019a) |
| 7 | Waste peanut hull powder (PHP biochar) | Conc.: 10-20mg/L, dose: 8g/L, time: 2h | 7 | 3.66 | (Kumar et al., 2019b) |
| 8 | Watermelon Rind (Citrullus lanatus) Biochar (WMRBC) | Conc. 1-100mg/L, dose: 8g/L, time: 3h | 1 | 9.5 | (Sadhu et al., 2021) |
| **Lanthanum Based Biochar** | | | | | |
| 9 | Lanthanum-loaded pomelo peel biochar (PPBC-La) | Conc.: 10-300mg/L, dose: 2g/L, time: 24h | 6.5 | 19.86 | (Wang et al., 2018) |
| 10 | Tamarix hispida biochar and lanthanum chloride (biochar–La) | Conc. 20-70mg/L, dose: 5g/L, time: 1.40h | 6 | 164.23 | (Habibi et al., 2019) |
| 11 | Aluminum/lanthanum-loaded wheat straw biochar (Al-La-WSB) | Conc.: 6-140mg/L, dose: 1g/L, time: 24h | 7 | 51.28 | (Yan et al., 2022) |
| 12 | La/Fe/Al oxides and rice straw biochar (La/Fe/Al-RSBC) | Conc.: 6-60mg/L, dose: 1g/L, time: 24h | 3-11 | 111.11 | (Zhou et al., 2022) |
| 13 | Lanthanum oxide nanoparticle–coated biochar (AcLaO) | Conc.: -, dose: 0.5g/L, time: - | 6 | 24.75 | (Chakraborty and Das, 2022) |
| **Lanthanum based adsorbents** | | | | | |
| 14 | Lanthanum-loaded magnetic cationic hydrogel composite (MCH-La) | Conc.: 0-80mg/L, dose: 0.3g/L, time: 24h | 7 | 136.78 | (Dong and Wang, 2016) |
| 15 | Magnetic magnesium–aluminum–lanthanum composite (Magnetic Mg–Al–La composite) | Conc.: 5-120mh/L, dose: -, time: 10h | 7 | 65.75 | (Zhao et al., 2017) |
| 16 | Lanthanum based nanoparticles L1 ($La(OH)_3$), L2 ($La_2O_3 \cdot nH_2O$) and L3 ($LaCO_3OH$) | Conc.: 5-50mg/L, dose: 0.5g/L, time: 3h | 3-9 | L1-6.03<br>L2-25.1<br>L3-28.9 | (Zhang et al., 2019b) |
| 17 | Lanthanum methanoate ($La(COOH)_3$) | Conc.: 10-80mg/L, 0.1g/L, time: 1.40h | 2-9 | 245.02 | (Yang et al., 2022) |
| 18 | Lanthanum-loaded watermelon rind biochar (3WMB-LN) | Conc.: 5-50mg/L, dose: 0.8g/L, time: 3h | 2 | 35.714 | This study |
| | | | 7 | 8.48 | |

"-" represents data not given in the references.

**4A.2.6. Effect of temperature:** The effect of temperature on fluoride uptake under optimized adsorption conditions of pH 3, dose 0.02g, equilibration time 180 minutes, and fluoride concentration 25 mg/L can be seen in **Figure 4A.3(d)**. It is evident from data that the adsorption process was independent of temperature.

**4A.2.7. Effect of competing anions:** Natural water often contains several anions such as $HCO_3^-$, $Cl^-$, $SO_4^{2-}$, and $NO_3^-$, etc. **Figure 4A.6a** illustrates the evaluation of the influence of some selected co-existing anions (such as $Cl^-$, $NO_3^-$, $SO_4^{2-}$, $HCO_3^-$, $CO_3^{2-}$, and a mixture of all these anions) on fluoride adsorption by 3WMB-LN. Using 0.02 g of 3WMB-LN in a 25 mL solution containing 25 mg/L of fluoride and 25 mg/L of various anions, fluoride adsorption over 3WMB-LN was examined. Bicarbonate and sulfate anions decrease fluoride adsorption by about 15%.

**4A.2.8. Reuse of adsorbent and application on real water sample:** The desorption of fluoride ions adsorbed onto 3WMB-LN was investigated with 0.05, 0.1, and 0.5N NaOH and HCl solutions. It was observed that maximum desorption was achieved with 0.05N NaOH solution utilized for desorption which was equilibrated with 25 mg/L fluoride in order to carry out the reusability of the adsorbent. 0.05N NaOH solution was used for the desorption in order to evaluate the reusability of 3WMB-LN.

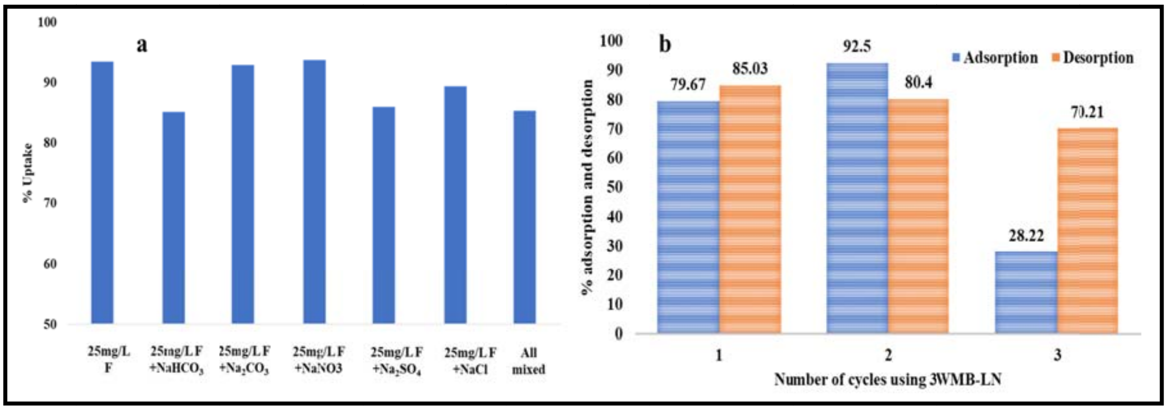

**Fig. 4A.6 (a)** Uptake of fluoride after consecutive 1st 2nd and 3rd cycles using 0.05N NaOH as regenerant (Initial dose: 0.02 g, pH 3, initial fluoride concentration: 25 mg/L, volume 25mL), b) Effect of competing anion concentration on % uptake of fluoride.

Further, three sequential adsorption-desorption cycles were performed in order to study the reusability of 3WMB-LN. Desorption was found out to be 85.03, 80.4, and 70.21% for the first, second, and third cycles, respectively, using 0.05N NaOH solution. The percent uptake of fluoride was observed to be 79.67%, 92.50%, and 28.22%, respectively, for the first, second, and third cycles of batch operations **(Figure 4A.6b).** Adsorption increased by 12.83% in the second cycle, which was due to NaOH's activation of the adsorbent. This adsorbent has been employed on a real water sample to ensure Zr-CH adsorbent's actual use and efficacy, by using groundwater samples collected from the MSU, Baroda Environmental Studies Department, and analyzed for its physicochemical parameters which are described in chapter **Table 3A.5**

The groundwater sample was spiked with standard fluoride solution (5, 15, and 25 mg/L)and the adsorption was carried out at optimized conditions without changing the pH (7.37) of the water sample. It was observed that fluoride could be removed up to 37.68% from groundwater which was spiked with 5mg/L fluoride solution and further decreased with increased presence of fluoride. The concentration of fluoride could be brought down to permissible limits. However, the removal was effective in acidic conditions.

## 4A.3. Characterization of 3WMB-LN and after adsorption of fluoride (3WMB-LNF)

**4A.3.1. TGA:** The sample was heated to temperatures between 30 and 560 degrees Celsius (**Figure 4A.7**). The first weight loss of 24.52% was seen in the TGA of 3WMBP-LN at ≈180°C, which could be attributed to the loss of water and moisture content. The second stage weight loss of 7.44% at temperatures 250-375°C was attributed to the decomposition of volatile matter, cellulose, hemicellulose, and lignin components (El-Nemr et al., 2022; Sadhu et al., 2021) followed by 13.6% weight loss in the temperature range of 375- 550°C due to the complete decomposition of organic matter leaving a probable residue that may include fixed carbon and lanthanum oxides.

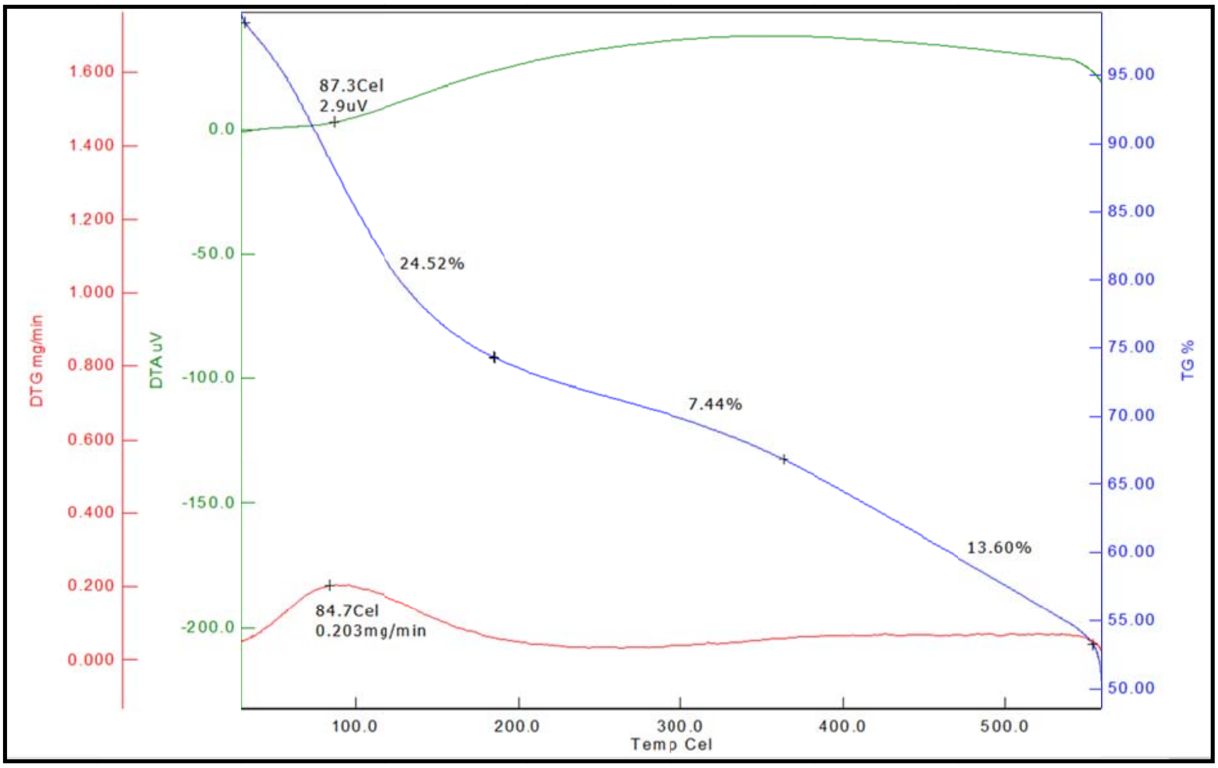

**Fig. 4A.7.** TGA graph of 3WMBP-LN

**4A.3.2. FTIR: Figure 4A.8** displays the FTIR spectra of the 3WMB-LN and 3WMB-LNF. The N-H and RCOOH bonds were represented by the broad band at 3328.56 $cm^{-1}$. The bands at 2959.63 $cm^{-1}$ and 2924.6 $cm^{-1}$ were attributed to the C-H stretching vibration while the peak at 1723 $cm^{-1}$ was caused by C=O and C=Vibrations (Li et al., 2022). The band at 1496.36 $cm^{-1}$ was attributed to C-O stretching while the band at 1394.52 $cm^{-1}$ was due to the vibration of $NO_3^-$, from $La(NO_3)_3$. Furthermore, the peak at 1071.73 $cm^{-1}$ was attributed to C-O-C stretching while 851.20 $cm^{-1}$ was ascribed to La-OH bond vibration. These IR spectral observations indicated that the lanthanum was impregnated with biochar (Wang et al., 2018). However, the disappearance of peaks at 851.20 $cm^{-1}$ and 1071.73 $cm^{-1}$ in 3WMB-LN after fluoride adsorption, suggested that there was an electrostatic interaction between the 3WMB-LN and fluoride ions (Li et al., 2024).

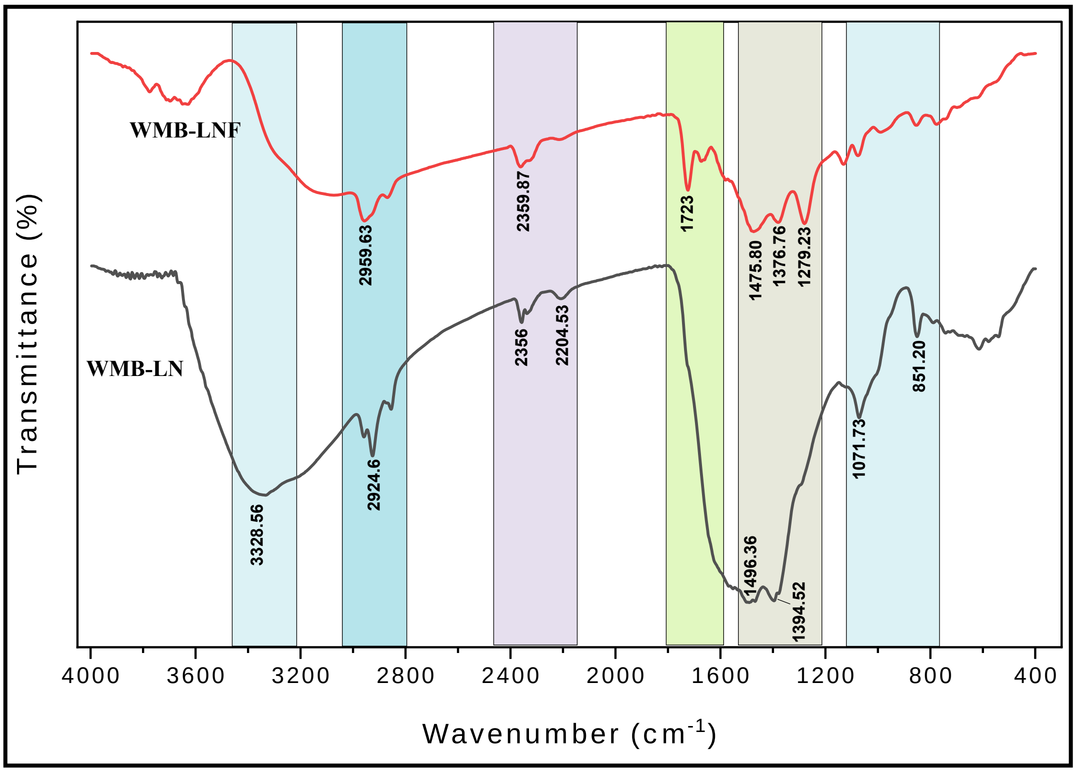

**Fig. 4A.8.** FT-IR spectra for 3WMB-LN and 3WMB-LNF

**4A.3.3. XRD: Figure 4A.9.** depicts the XRD spectrum of 3WMB-LN The slightly broad peak at approximately $15^0$ in the 3WMB-LN XRD pattern was ascribed to the aromatization and the graphitization of organic matter ( graphite 002) in biomass of watermelon rind and the peak at $21^0$ was assigned to quartz while the peak at ~$29^0$ was assigned to sylvite. There are many signals relating to LaOOH, LaONO$_3$, and La(OH)$_3$ because lanthanum was impregnated in biochar (Wang et al., 2016; Yan et al., 2022). The intensity of the peaks diminished in 3WMB-LNF, suggesting that fluoride had been adsorbed on this material **(Figure 4A.10.)**.

**4A.3.4. SEM and EDS: Figure 4A.10(a)** shows the SEM image of 3WMB-LN which revealed that it was fibrous with a fibrillar network of material that was observed to break down after fluoride adsorption. Additionally, **Figure 4A.10(a)** demonstrated that the 3WMB-LN displayed numerous brighter patches due to the loading of La complex particles, which was well supported by the 3WMB-LN's smaller surface area. The elemental composition before and after the adsorption process was also determined by energy-dispersive X-ray spectroscopy**.**

**In Figure 4A.10 (c)&(d)**, the elemental analysis results and EDX spectra of 3WMB-LN and 3WMB-LN after fluoride adsorption (3WMB-LNU) were displayed. From **Figure 4A.10 (c)&(d)**, two key things were implied: first, the presence of the lanthanum in the adsorbent suggests that the biochar has been successfully impregnated with La. Secondly, successful adsorption of fluoride (1.41%, ) was revealed by the presence of fluoride in EDX spectra of 3WMB-LNF after adsorption.

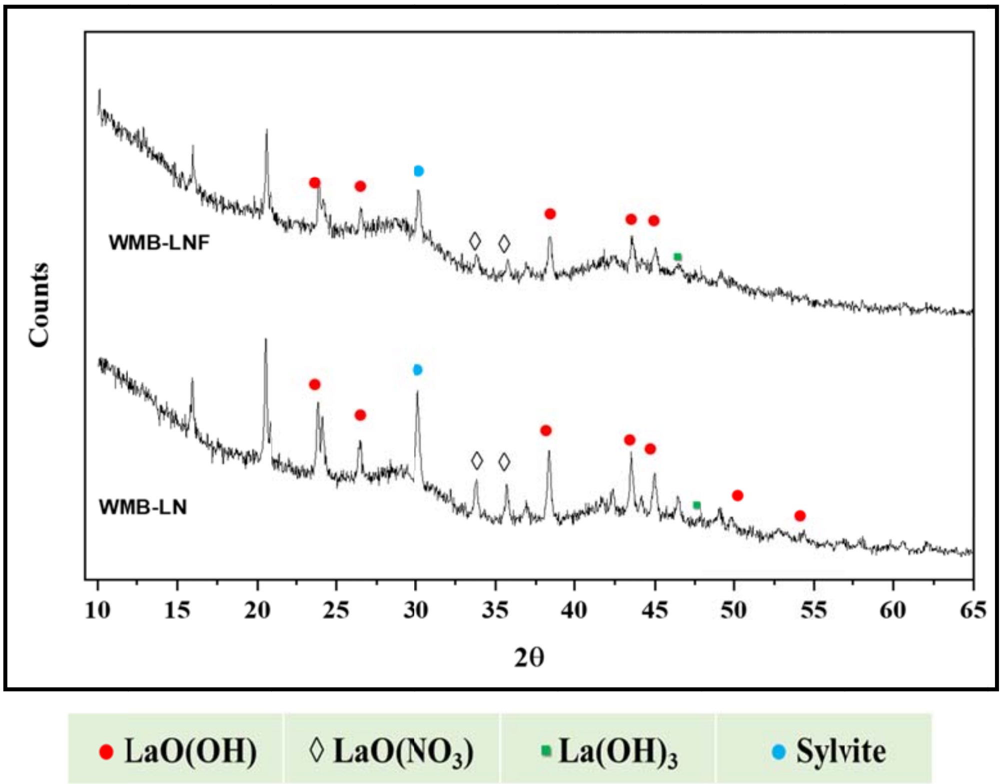

**Fig. 4A.9.** XRD spectra before and after fluoride adsorption on 3 WMB-LN

**4A.3.5. BET:** BET analysis validated the finding that after fluoride was adsorbed on 3WMB-LN, the surface area of the material decreased from 11.68 m$^2$/g to 10.83 m$^2$/g with an average pore diameter of 100.707Å and 119.214 Å for 3WMB-LN and 3WMB-LNF respectively. The surface area reduction and increase in pore size might be related to the adsorption of fluoride as lanthanum fluoride leading to the widening of micropores.

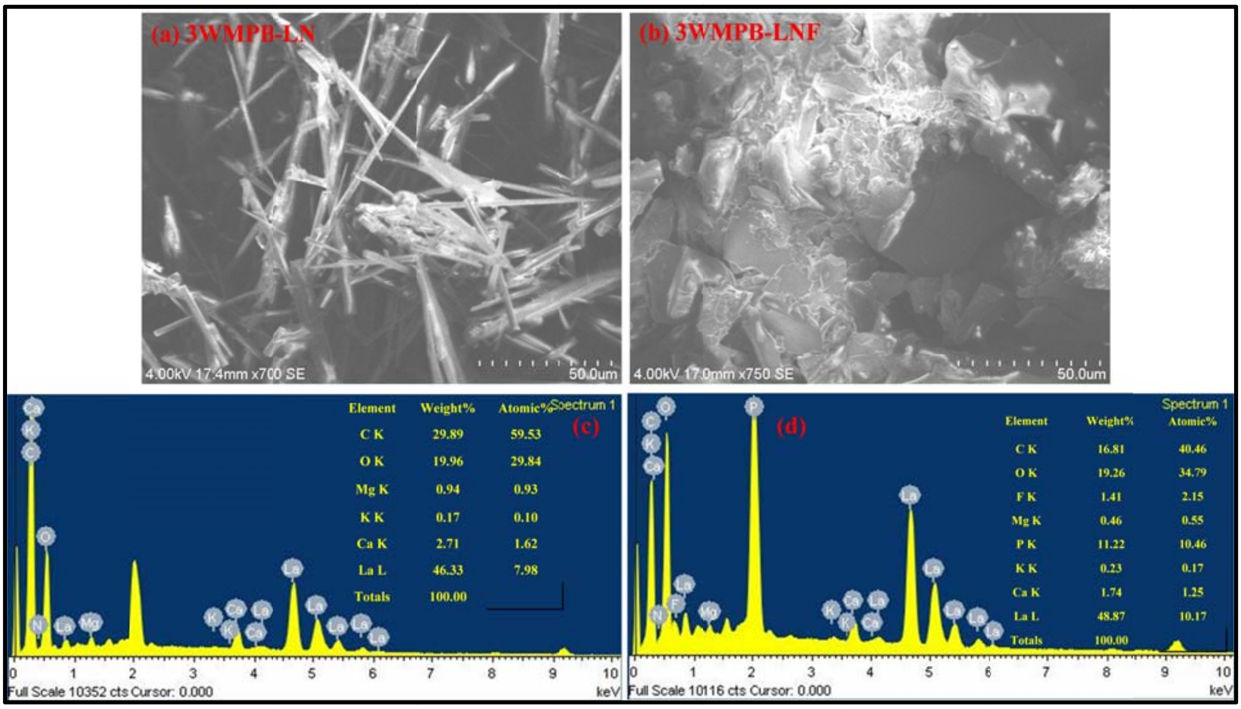

| Element | Weight% | Atomic% |
|---|---|---|
| C K | 29.89 | 59.53 |
| O K | 19.96 | 29.84 |
| Mg K | 0.94 | 0.93 |
| K K | 0.17 | 0.10 |
| Ca K | 2.71 | 1.62 |
| La L | 46.33 | 7.98 |
| Totals | 100.00 | |

| Element | Weight% | Atomic% |
|---|---|---|
| C K | 16.81 | 40.46 |
| O K | 19.26 | 34.79 |
| F K | 1.41 | 2.15 |
| Mg K | 0.46 | 0.55 |
| P K | 11.22 | 10.46 |
| K K | 0.23 | 0.17 |
| Ca K | 1.74 | 1.25 |
| La L | 48.87 | 10.17 |
| Totals | 100.00 | |

**Fig. 4A.10**. **(a)** & **(b)** SEM images and **(c)** & **(d)** EDS graphs of 3WMB-LN and 3WMB-LNF

**4A.3.6. XPS:** To understand the adsorption mechanism in detail, the XPS spectra **(Figure 4A.11)** of 3WMB-LN was compared with 3WMB-LNF. The XPS survey spectrum of the 3WMB-LN, and 3WMB-LNF as shown in **Figure 4A.11(a),** which clearly showed the presence of lanthanum, carbon, nitrogen, and oxygen. After the fluoride adsorption, a new peak at about 684.79 eV attributed to F1s (Jia et al., 2015; Wang et al., 2018) was observed. In the case of 3WMB-LN, the atomic percentage distribution was found to be 40.69% for La3d, 23.82% for O1s, 3.24% for N1s, 18.86% for C1s and 13.39% for La4d. Whereas after adsorption of fluoride, the atomic percentage distribution found in 3WMB-LNF was 42.72% of La3d, 2.12% of F1s, 19.66% of O1s, 2.47% of N1s, 18.76% of C1s, and 14.27% of La4d. The deconvoluted spectra of F1s as seen in **Figure 4A.11(h)** showed a single component with a peak at 684.79 which could be attributed to LaOF formation (Barreca et al., 2005). **Figures 4A.11(c&g)** correspond to the XPS spectra of La3d before and after fluoride adsorption respectively. La3d$_{5/2}$ peaks were observed at 835.45 eV and 838.73 eV, while La3d3/2 for the pristine 3WMB-LN were centered at 855.55 eV and 852.25 eV. The La3d$_{5/2}$ after adsorption shifted to 835.38eV and 838.43 eV while the La3d$_{3/2}$ peaks shifted to 838.43 and 855.46 showing a slight change in the binding energy. This could be due to the development of a new La species and the transfer of valence electrons from La3d (Wang et al., 2018). The C1s spectra before adsorption **(Figure 4A.11(b))** display signals corresponding to 286.08 which may be attributed to the C=O/C-N bond. The deconvoluted spectra post adsorption as seen in

**Figure 4A.11(f)** the peaks were found at 288.46 eV and 285.95 eV. The deconvoluted spectra of O1s before adsorption **(Figure 4A.11(d))** exhibited peaks at 531.49 eV, 532.89 eV, and 529.95 eV which could be attributed to the C=O, C-O, and M-oxide respectively. Post adsorption the deconvoluted spectra of O1s as seen in **Figure 4A.11(i)** showed two peaks mainly at 532.23 and 531.02 which again could be attributed to the C=O and C-O bonds respectively. The N1s spectra before adsorption **(Figure 4A.11(e))** exhibited peaks at 399.40 eV and 403.82 eV assigned to pyrrolic and pyridinic N respectively. These peaks post adsorption shifted to 399.89 and 398.10 eV respectively as seen in **Figure 4A.11(j)**. **Figure 4A.12** shows the plausible mechanisms of fluoride adsorption on 3WMB-LN adsorbent.

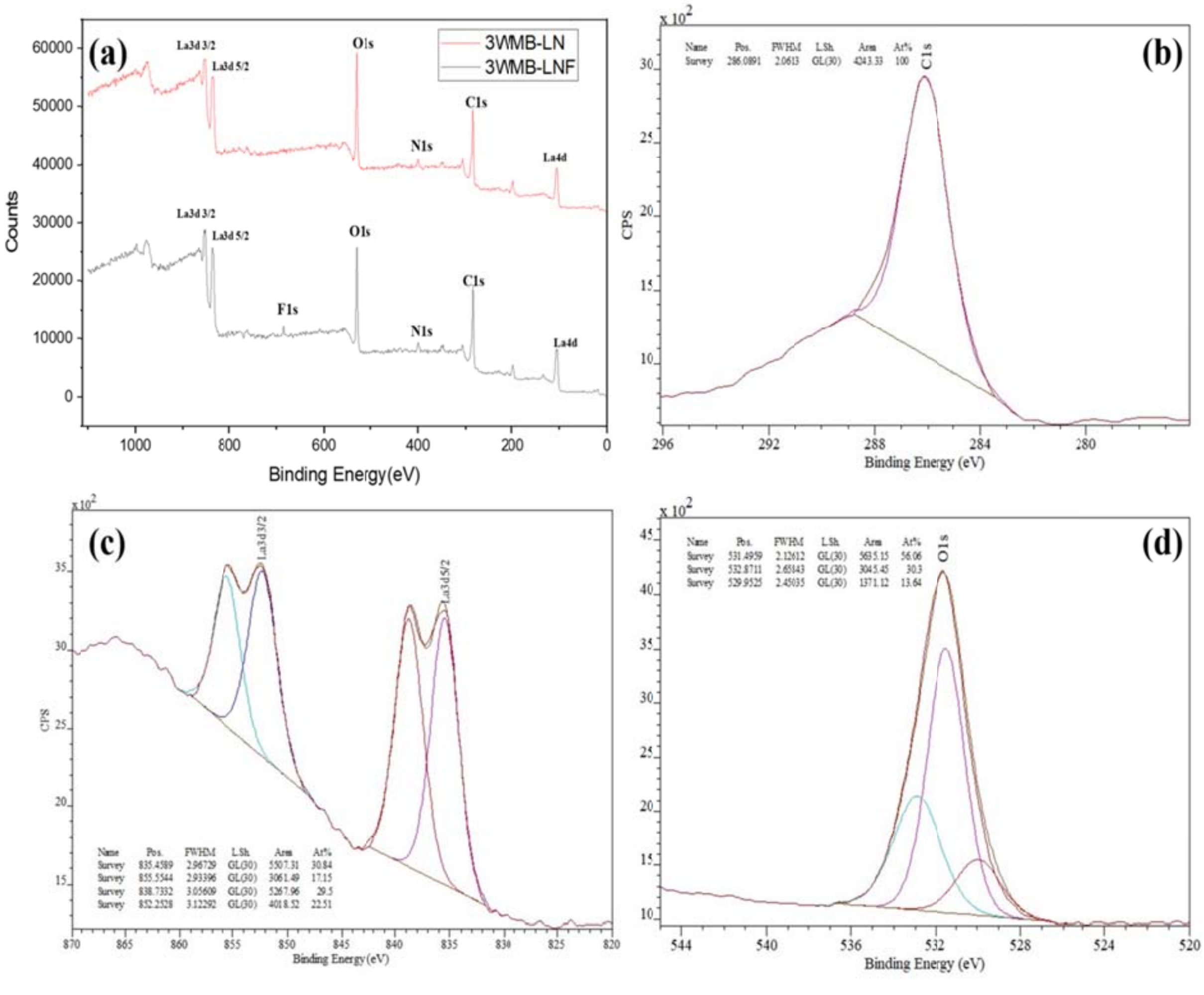

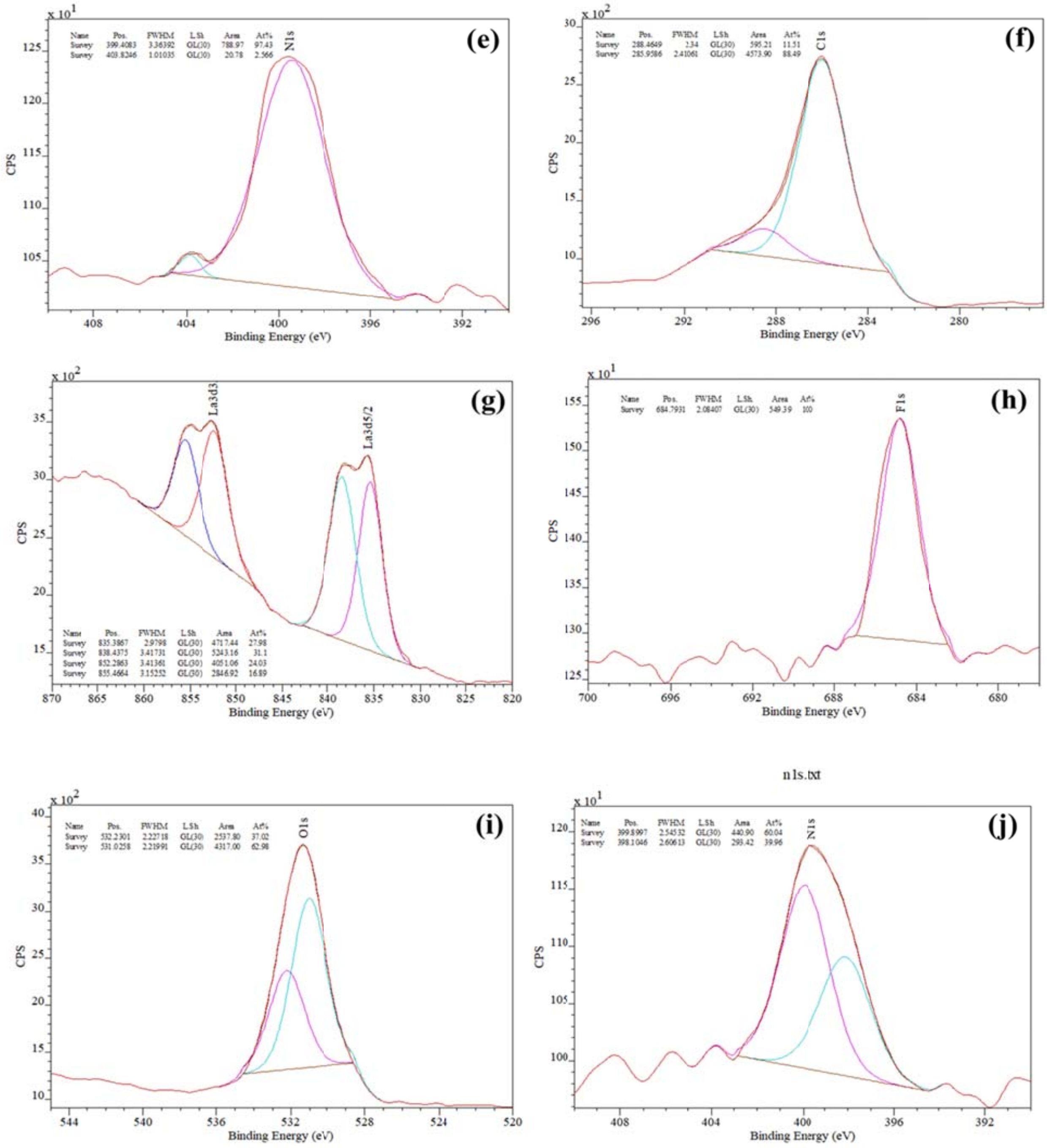

**Fig. 4A.11 (a)**Survey spectrum of 3WMB-LN and 3WMB-LNF, **(b)** deconvoluted peak of C1s of 3WMB-LN, **(c)** deconvoluted peak of La3d of 3WMB-LN, **(d)** deconvoluted peak of O1s of 3WMB-LN, **(e)** deconvoluted peak of N1s of 3WMB-LN, **(f)** deconvoluted peak of C1s of 3WMB-LNF, **(g)** deconvoluted peak of La3d of 3WMB-LNF, **(h)** deconvoluted peak of F1s of 3WMB-LNF, **(i)** deconvoluted peak of O1s of 3WMB-LNF, and **(j)** deconvoluted peak of N1s of 3WMB-LNF.

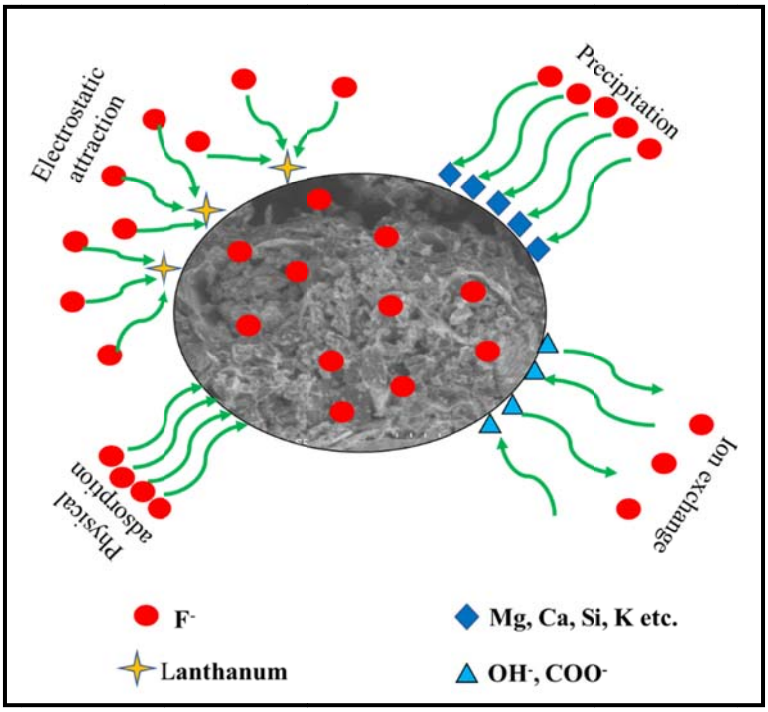

**Fig. 4A.12.** Plausible mechanism of fluoride adsorption on 3WMB-LN.

## Conclusion

Lanthanum-modified watermelon rind biochar was synthesized and characterized by different techniques such as FT-IR, XRD, BET, SEM-EDS, XPS, and TGA. Lanthanum was successfully impregnated in biochar as indicated by XRD data. From these techniques, it was also concluded that fluoride was adsorbed on 3WMB-LN through electrostatic interaction between 3WMB-LN and $F^-$ ions, as well as ion exchange with $OH^-$ and $COO^-$ groups along with precipitation of K, Mg, Ca, etc.  Pseudo-second-order kinetic and Langmuir isotherm models provided the best fit suggested chemisorption and monolayer adsorption of fluoride on 3WMB-LN respectively. The maximum adsorption capacity of 3WMB-LN at optimum pH 3 was 35.71 mg/g, which is superior to previously reported watermelon rind biochar removal of fluoride. Temperature fluctuations had little impact on this investigation. The adsorption capacity of 3WMB-LN was unaffected by common co-existing anions such as carbonate, nitrate, and chloride, however, the presence of bicarbonate and sulfate affected the adsorbent's adsorption capacity a little (~8%). After two cycles, the regeneration findings verified that 92.5% of the initial adsorption capacity was still retained. The method investigated showed that by electrostatic attraction, lanthanum made the largest contribution to fluoride adsorption. In conclusion, the 3WMB-LN provides advantages in real-world applications and is inexpensive, environmentally friendly, and effective.

# Chapter 4B

## Preparation and Synthesis of Zirconium Cholate (Zr-CH) Adsorbent for the Removal of Fluoride from Aqueous Solution

### 4B.1. Materials and Experimental Methodology

**4B.1.1. Materials and chemicals:** The chemicals zirconyl chloride octahydrate ($ZrOCl_2.8H_2O$) and cholic acid sodium salt ($C_{24}H_{39}NaO_5$) which is also known as sodium cholate of SRL were utilized to fabricate Zr-CH. NaF from SRL, NaOH, and HCl were employed to maintain the pH of the solution. The regeneration of Zr-CH also involved the use of sodium hydroxide.

**4B.1.2.Synthesis of Zirconium cholate (Zr-CH):** The solutions of zirconium chloride (1M) and sodium cholate (3M) were mixed in a 1:3 (v/v) ratio and heated on a hot plate till boiling to precipitate zirconyl cholate (Zr-CH). After heating, the solution was cooled at room temperature and filtered through the Whatman 41 filter paper, and the precipitate was washed until the pH was neutral and dried at 90°C in a hot air oven before being stored in an airtight container for further use. The methodology used for the preparation and synthesis of Zr-CH adsorbent is depicted in the flow chart below **(Figure 4B.1).**

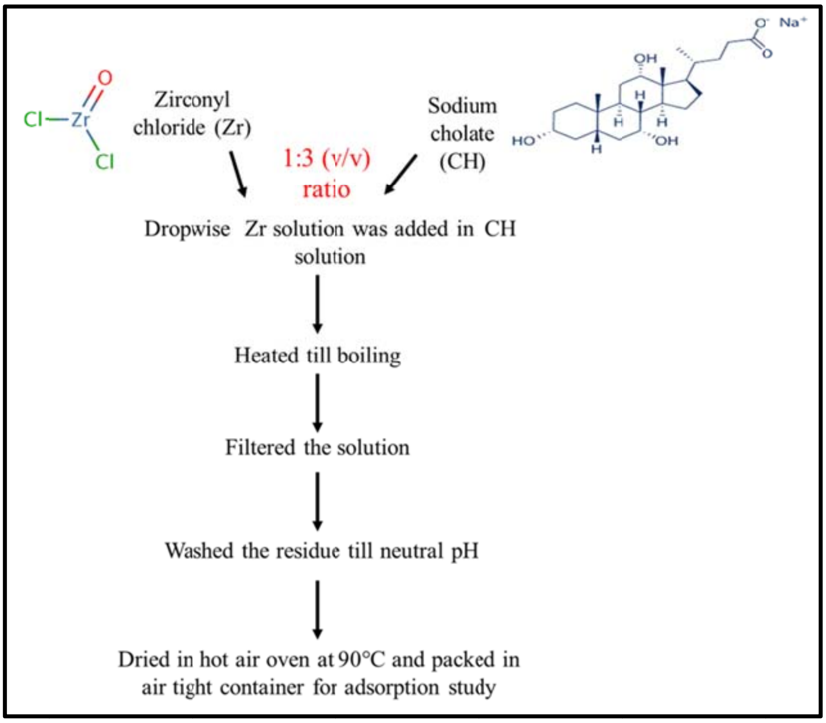

**Fig. 4B.1**. Methodology for preparation of Zr-CH

**4B.1.3. Batch experiment for fluoride uptake:** By using a batch adsorption procedure, the adsorptive capability of Zr-CH for fluoride removal was studied. 0.1M NaOH and HCl were used to maintain the pH of the solution to the appropriate level. For the batch experiments, polypropylene conical flasks containing 0.1 g of Zr-CH was equilibrated with 25 mg/L of a fluoride-containing 25mL solution at 150 rpm for three hours at room temperature (25–30ºC). The adsorbent was filtered and dried after fluoride uptake for further characterization.

## 4B.2.Results and discussion

**4B.2.1. pH variation study:** Due to the protonation-deprotonation of the cations in the host layer, the pH of the initial solution affects the surface charge of Zr-CH (Zhang et al., 2012). **Figure 4B.2** shows that the amount of fluoride adsorption reduced from 93.96% to 69.9% when pH values increased from 2 to 10. This may be because, at higher pH levels, hydroxyl ions and fluoride ions will compete for the same active adsorption sites (Zhu et al., 2015). Due to the electrostatic interaction between fluoride and Zr-CH, the highest removal of fluoride occurred at pH 2, indicating that removal at low pH was favorable. Further studies such as optimization of dose, concentration, and time were carried out at neutral pH as well as pH 2 considering that there was 75% removal and would be more amenable for practical application of groundwater.

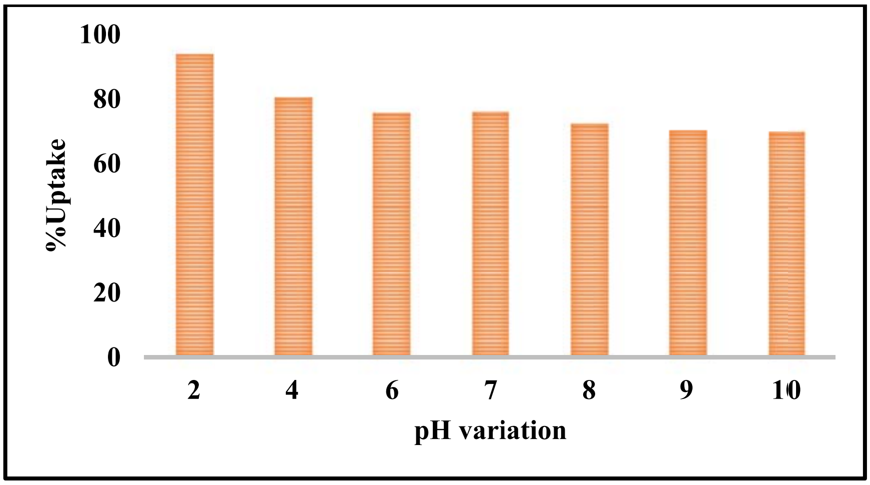

**Fig. 4B.2**. The effect of pH on percentage uptake of fluoride onto Zr-CH (time;180minutes. dose;0.1g, conc.;25mg/L, volume; 25mL, temp: 25-30ºC).

**4B.2.2. Effect of dose variation: Figure 4B.3** shows the results of the dose variation study conducted at both neutral pH and the optimal pH (2pH) with varying doses of 0.05 to 0.1g ZrCH. It was observed that the percent of fluoride uptake at both pH levels increased as the

Zr-CH dose increased. When the adsorbent dose was increased, the availability of vacant sites for the uptake of fluoride increased, which accounts for the observed increased fluoride removal efficiency with increased dosage for both pH levels. 100mg of ZrCH was used in further studies.

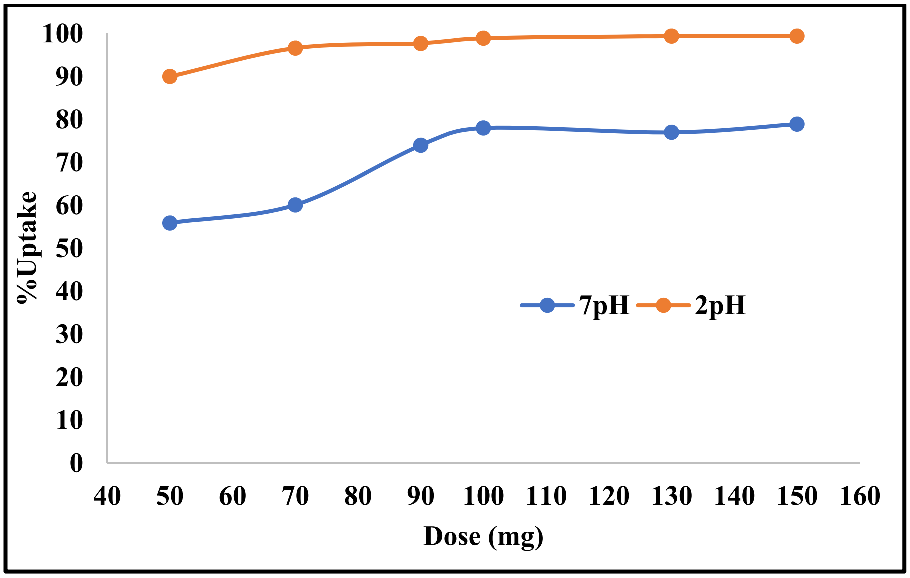

**Fig. 4B.3.** Effect of dose variation on % uptake of fluoride on Zr-CH (time: 180min, conc.: 25mg/L).

**4B.2.3. Concentration variation and isotherm study:** The effect of the initial fluoride concentration on the absorbent's capacity to adsorb can be observed in **Figure 4B.4**. at both neutral pH and 2 pH.

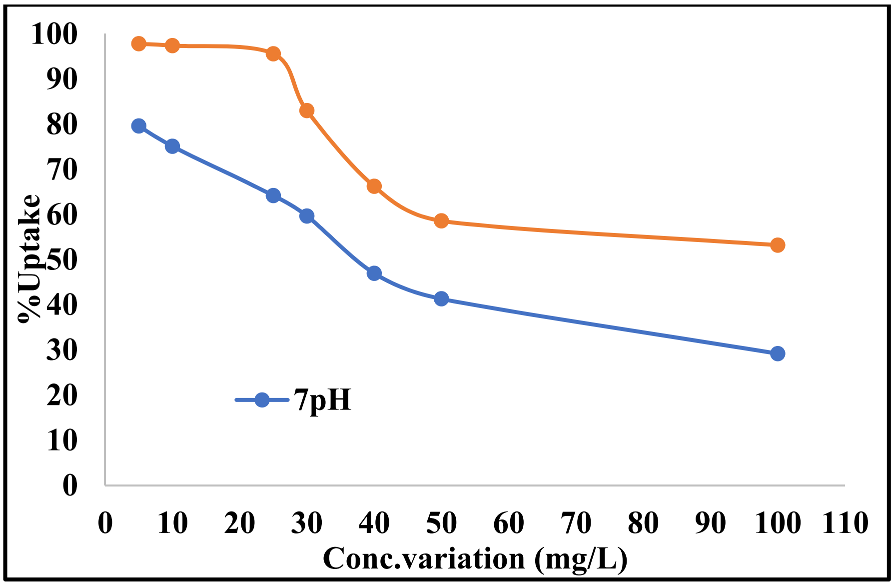

**Fig. 4B.4** Fluoride adsorption percentage and initial fluoride concentration effects at neutral and 2 pH (time: 3 h, dose: 0.1g)

The Langmuir and Freundlich models at pH 2 and 7 are shown in **Figure 4B.5 a, b, c, and d.** While Freundlich's isotherm assumes that adsorption takes place on the heterogeneous surface of the adsorbent, Langmuir's isotherm describes the monolayer adsorption of fluoride onto the Zr-CH surface having a finite number of adsorption sites.

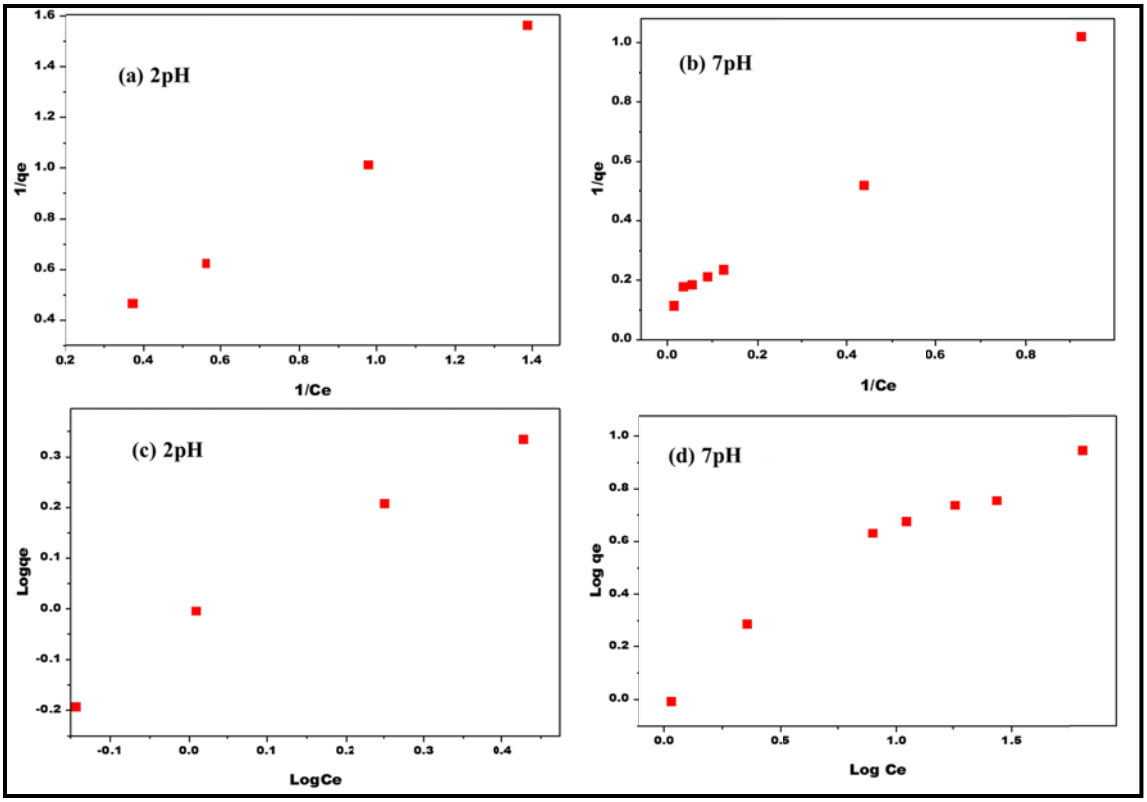

**Fig. 4B.5**. **(a)** & **(b)** Langmuir plots for Zr-CH at 2 and 7pH respectively, and **(c)** & **(d)** Freundlich plots at 2 and 7 pH respectively.

The results shown in **Table 4B.1** indicated that Langmuir's isotherm was the best fitted because the $R^2$ value at both 2 pH and neutral pH ($R^2 = 0.991$ and 0.996 at 2 and neutral pH respectively) was greater than 0.99 in contrast to Freundlich isotherm ($R^2 = 0.911$ and 0.95 for all cases) suggesting the monolayer adsorption of fluoride on Zr-CH. At neutral pH and 2 pH, respectively, the maximum fluoride adsorption capacity of Zr-CH was found to be 8.40 mg/g and 37.04 mg/g. In **Table 4B.2**, the literature-reported fluoride adsorption capacities of Zr-CH and various other adsorbents are compared.

**Table 4B.1.** Isotherm parameters of Zr-CH

| Isotherm models | Isotherm parameters | | |
|---|---|---|---|
| | | **2pH** | **7pH** |
| **Freundlich isotherm** | **$K_f$ (L.g$^{-1}$)** | 1.09 | 1.18 |
| | **1/n** | 0.91 | 0.51 |
| | **$R^2$** | 0.985 | 0.95 |
| **Langmuir isotherm** | **$q_{max}$ (mg/g)** | 37.04 | 8.40 |
| | **$K_L$ (L. mmol$^{-1}$)** | 0.026 | 0.14 |
| | **$R^2$** | 0.988 | 0.996 |

**Table 4B.2.** Literature Review for fluoride removal using Zirconium based adsorbents

| Raw Materials and adsorbents name | Dose (gm) and Conc. (mg/L) | pH | Qmax (mg/g) | References |
|---|---|---|---|---|
| Zirconium-based metal-organic framework (MOF-801) | Dose:1g/L, Conc.:5-25mg/L | - | 19.42 | (Tan et al., 2020) |
| Valence orange (*Citrus sinensis*) and Red Delicious apple (*Malus Domestica*) peels impregnated with zirconium (BOP-Zr and BAP-Zr) | Dose:1g/L, Conc.: 2-10mg/L | 3.5 | 4.854(BOP-Zr) and 5.627(BAP-Zr) | (Robledo-Peralta et al., 2022) |
| $Al_2O_3$–$ZrO_2$ adsorbent | Dose:1g/L, Conc.: 50-120mg/L | 2 | 114.54 | (Zhu et al., 2015) |
| Zirconium-impregnated graphene oxide-coated sand, (ZIGCS) | Dose:2g/L, Conc.: - | 4 | 6.12 | (Prathibha et al., 2020) |
| Zirconium-chitosan/graphene oxide (Zr-CTS/GO) | Dose: 3g/L, Conc.: - | 3-11 | 29.05 | (Zhang et al., 2017) |
| Mg-Al-Zr composite (Mg-Al-Zr) | Dose: 1g/L, Conc.: - | 7 | 22.9 | (Wang et al., 2017) |
| Zirconium-modified activated carbon fibers (Zr-AC) | Dose: 2g/L, Conc.: - | 7 | 28.5 | (Pang et al., 2020) |
| layered Zr-Al-La composite (AZL) | Dose: 0.5g/L, Conc.: 20-140mg/L | 3 | 90.48 | (Zhou et al., 2018) |
| Zirconium-graphene hybrid adsorbent [$(ZrO(OH)_{1.33}Cl_{0.66}$-reduced graphene oxide (rGO)]. | Dose: 0.75g/L, Conc.: 10-500mg/L | - | 44.14 | (Zhang et al., 2019a) |
| Mesoporous zirconium pyrophosphate (ZPP) adsorbents | Dose: 0.2g/L, Conc.: - | 7 | 34.30 mmol/g | (Chen et al., 2022) |
| Zirconium cholate (Zr-CH) | Dose:4g/L, Conc.5-100mg/L | 7 | 8.40 | Present study |
| | | 2 | 37.04 | |

"-" represents, data not given properly in reference.

**4B.2.4. Time study and adsorption kinetics:** The fluoride adsorption kinetics was studied by equilibrating 25 mL of a solution containing 10 mg/L of fluoride at optimum pH conditions for various time intervals with 0.1g of Zr-CH, (**Figure 4B.6**). Fluoride was significantly removed in the first 30 minutes (88%), with a slower returned to equilibrium over120 minutes. In the presence of a large solute concentration gradient, the initial quick adsorption may be caused by vacant adsorption sites, while the subsequent slow rate may be caused by saturation of the available adsorption sites (He et al., 2019).

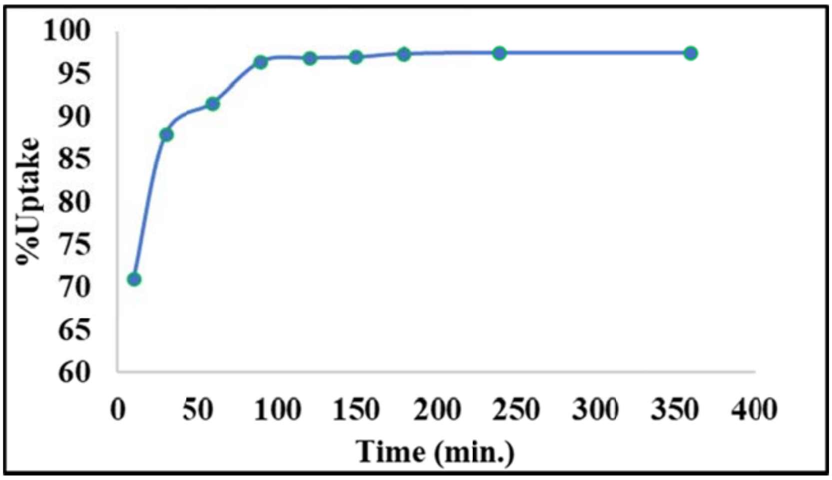

**Fig. 4B.6.** Effect of contact time on % uptake of fluoride (pH 7, conc. 10mg/L, dose: 0.1g)

**Figure 4B.7** illustrates the fitting of adsorption data to the pseudo 1st and pseudo 2nd-order kinetic models. **Table 4B.3** lists the results of the fitting of two kinetic models to the fluoride equilibrium data and the values of the corresponding kinetic parameters. The higher value of the linear regression coefficient ($R^2 > 0.999$) for the pseudo 2nd order model ($R^2 = 0.962$), suggested that pseudo 2nd order kinetics was the best-fitted model for describing the kinetics of fluoride adsorption on Zr-CH. Further, there is a rational agreement between the calculated and experimental adsorption capacity (qe) values indicating that the adsorption process was chemisorption (Tan et al., 2020).

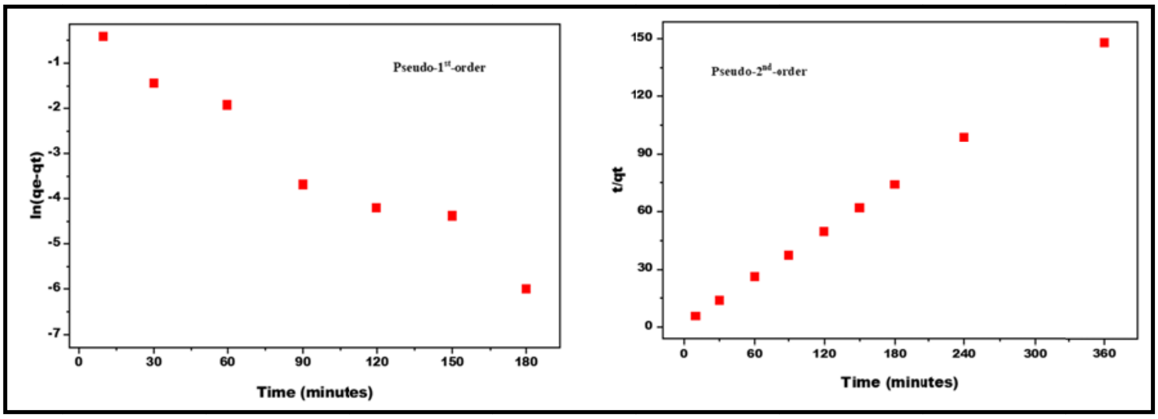

**Fig. 4B.7.** Kinetics plots of Zr-CH adsorbent for fluoride removal

**Table 4B.3.** Kinetic parameters and their numeric value of Zr-CH

| Kinetic models | Kinetic parameters | Numerical value |
|---|---|---|
| **Pseudo -1st order** | **$K_1(min^{-1})$** | -0.00017 |
| | **qe(mg/g)** | 0.702 |
| | **$R^2$** | 0.962 |
| **Pseudo- 2nd order** | **$K_2(gmg^{-1}\ min^{-1})$** | 0.13 |
| | **qe, cal (mg/g)** | 2.46 |
| | **qe, exp(mg/g)** | 2.44 |
| | **$R^2$** | 1.00 |

**4B.2.5. Effect of competing anions:** Apart from the cations of interest, numerous additional anions are typically present in groundwater, wastewater streams, and other sources of drinking water. Therefore, from the application point of view, it is particularly desirable to investigate fluoride uptake in the presence of other anions. Using a 4 g/L adsorbent dose in a 10 mg/L fluoride solution including -10 mg/L anions such as chloride, sulfate, nitrate, carbonate, and bicarbonate as well as a mixture of these anions, fluoride uptake at pH 7 was investigated. The same amounts of fluoride and all anions (10 mg/L for each) were used in the mixed solution. The effects of anions on the fluoride adsorption efficiency using Zr-CH are shown in **Figure 4B. 8**. **Figure 4B.8** indicates evidence that the presence of carbonate and bicarbonate decreased the adsorption efficiency by about 9% while nitrate, sulphate, and chloride did not interfere.

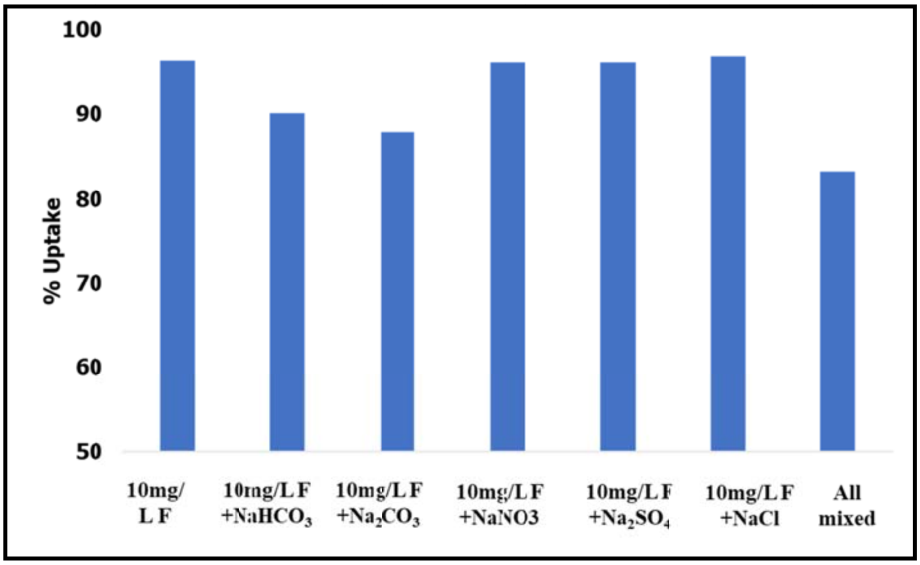

**Fig. 4B.8.** Influence of fluoride adsorption percentage and competing anion concentration (parameters; pH-7, dose-0.1g, conc.-10mg/L, each of fluoride and competing anions under study, volume; 25mL and time- 3h)

**4B.2.6. Reuse of adsorbent and application on real water sample:** The desorption of fluoride ions adsorbed onto Zr-CH was investigated with 0.05, 0.1, and 0.5N NaOH and HCl solutions. It was observed that maximum desorption was achieved with 0.05N NaOH solution utilized for desorption which was equilibrated with 10 mg/L fluoride in order to carry out the reusability of the adsorbent. 0.05N NaOH solution was used for the desorption to evaluate the reusability of Zr-CH. For this, desorption was carried out (with 0.05 N NaOH), then the adsorbent was dried. The adsorbent was then put to use another time. For three cycles, the percentage uptake of fluoride was determined to be 94.25%, 95.36%, and 14.11%, respectively **(Figure 4B.9)**. It was found that the material could be reused for a maximum of two cycles.

This adsorbent was also applied to real water samples in order to demonstrate the applicability and efficacy of Zr-CH. The groundwater sample was collected (Chapter 4A) and spiked with standard fluoride solution (5, 15, and 25 mg/L), and the adsorption experiment was conducted under optimal conditions without altering the pH of the real water sample. It was observed that for 5mg/L of fluoride concentration, 75% of fluoride could be removed using ZrCH as an adsorbent.

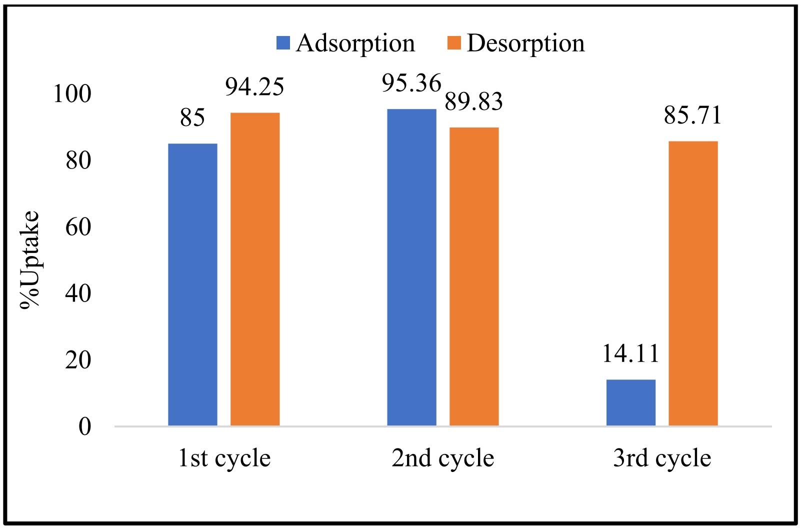

**Fig. 4B.9.** Uptake of fluoride after consecutive 1st 2nd and 3rd cycles using 0.05N NaOH as regenerant (Initial dose: 0.1 g, pH 7, initial fluoride concentration: 10 mg/L, volume 25mL).

## 4B.3.Characterization of Zr-CH before and after fluoride adsorption on Zr-CH (Zr-CHF)

**4B.3.1. FTIR:** The FTIR spectra of ZrCH exhibited peaks representative of both sodium cholate and Zirconyl. The peaks observed at 909.25 cm$^{-1}$ attributed to trans-CH wag, 978.35 cm$^{-1}$ attributed to Zr-O stretch, 1073.68 cm$^{-1}$ attributed to C-O stretch, 1196.31 cm$^{-1}$(C-C/ Zr-O-C stretch), 1308 cm-1 to bending vibration of Zr-OH groups 1444.22 cm$^{-1}$ attributed to antisymmetric methyl deformation, 1568.22 cm$^{-1}$ was assigned to antisymmetric COO stretching, 1705.13 cm$^{-1}$ attributed to C=O stretch, 2668.24 cm$^{-1}$ attributed to vibration of hydroxyl bond (OH) of the carboxylic acid, 2934.13 cm$^{-1}$ assigned to CH stretching and 3395.41 cm$^{-1}$ assigned to OH groups were characteristic to cholate **(Figure 4B.10)**. As shown in **Figure 4B.10,** no change was found in the FTIR spectra and all the characteristic peaks still exist without the rise of new peaks. However, Zr–F stretching and F–Zr–F bending vibration occurs in the far infra-red region, which could not be observed (Dou et al., 2012). This confirmed the reliable stability of the Zr-CH metal framework throughout the adsorption process. A similar study was reported by Hossien and his colleagues for the organic metal framework (Hossien Saghi et al., 2021).

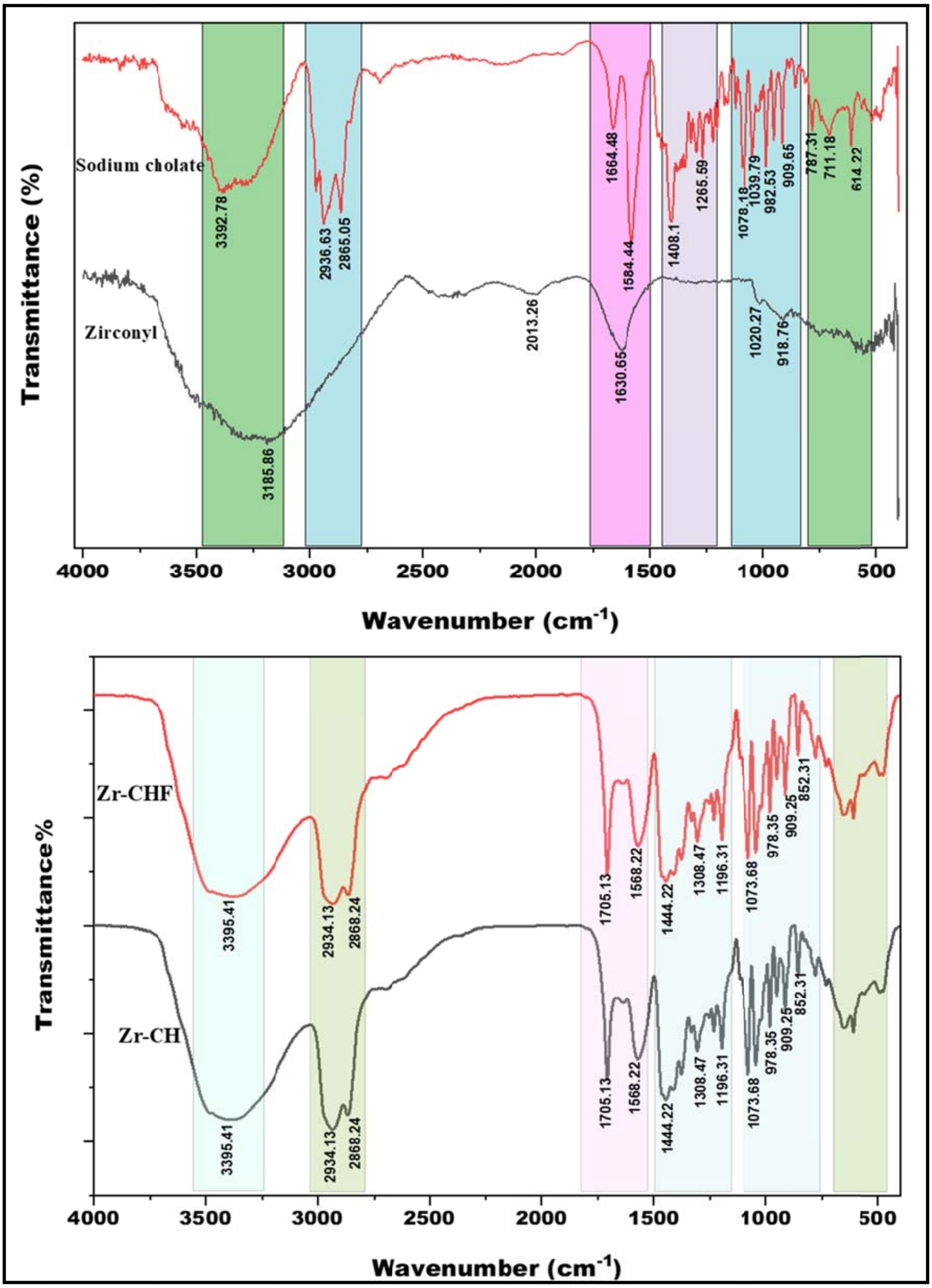

**Fig. 4B.10.** FT-IR spectra for sodium cholate, zirconyl, and Zr-CH before and after adsorption of fluoride.

**4B.3.2. XRD:** XRD was used to examine the materials' phase purity. Furthermore, the acquired peak intensity was high, indicating strong crystallinity, and no other XRD peaks were seen, demonstrating that Zr-CH MOF was successfully synthesized (Tan et al., 2020). MOFs have peaks at angles 8°, 12.2°, 17.5°, and 23.1°which correspond to the (0 0 1), (0 2 2), (0 0 4), and (1 1 5) planes **(Figure 4B.11c).** These peaks represent the character of the diffraction pattern of Zr-BDC (UiO-66) and other MOFs (Gwardiak et al., 2019).

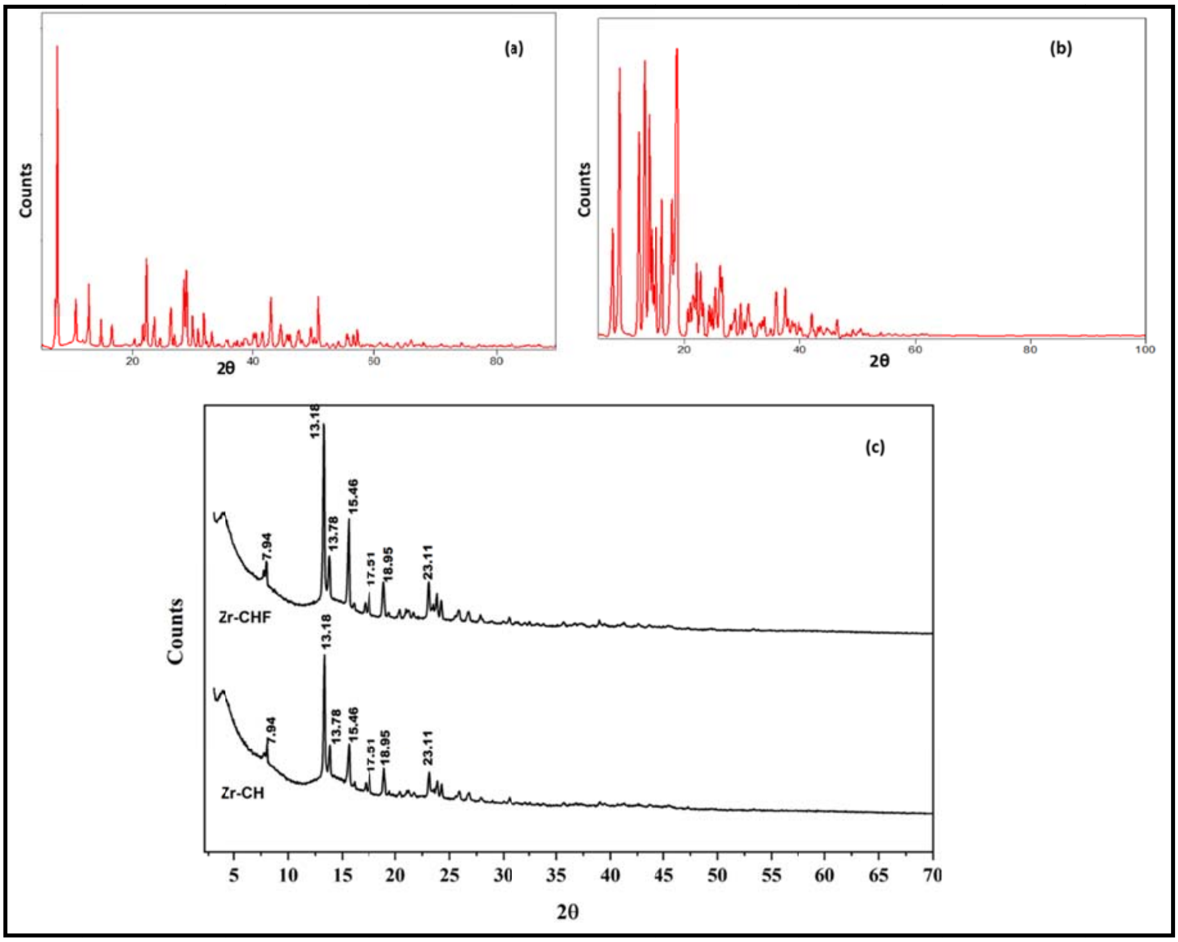

**Fig. 4B.11.** XRD spectra of (a) Zirconyl chloride, (b) Sodium cholate, and (c) Zr-CHF and Zr-CH.

**4B.3.3. SEM-EDS:** SEM images of Zr-CH and Zr-CHF are depicted in **Figures 4B.12 a&b**. The images suggested the crystalline nature of ZrCH and that the crystalline nature was retained after the adsorption of fluoride (**Figures 4B.12 (c)&(d))** depicts the Zr-CH adsorbent's EDS spectra both before and after fluoride adsorption.

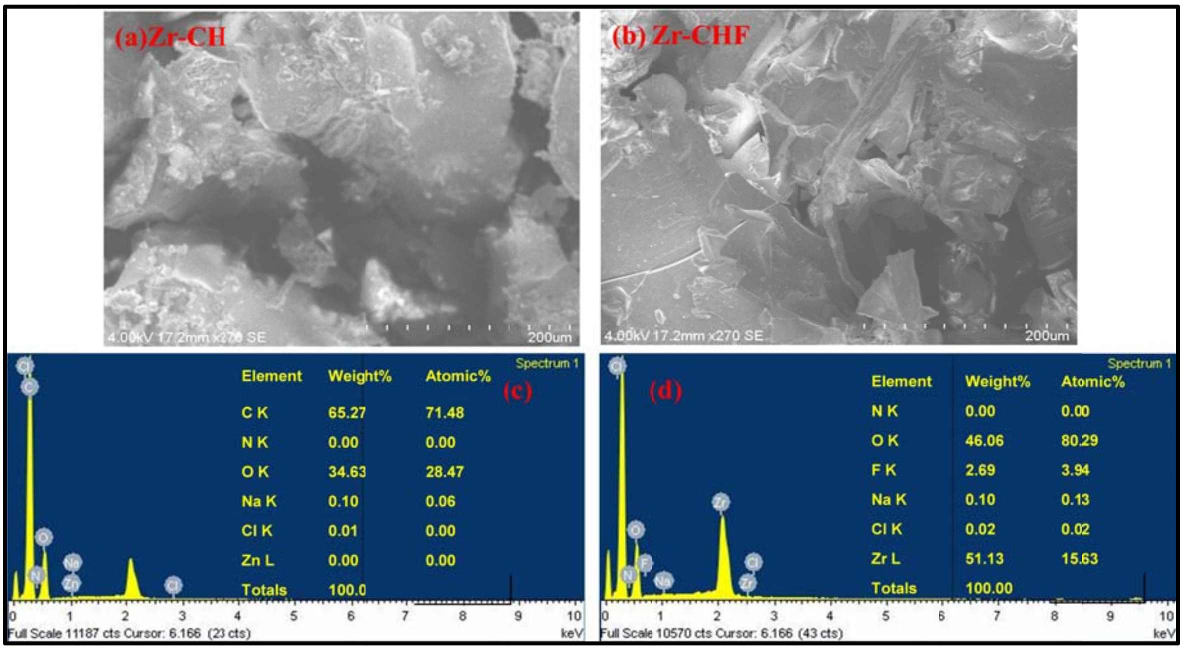

**Fig. 4B.12. (a)** and **(b)** SEM images of Zr-Ch and Zr-CHF, (c)&(d) EDS of Zr-CH and Zr-CHF.

**4B.3.4. TGA:** The weight loss of 15.2% at ≈200ºC was seen in the Zr-CH thermogram **(Figure 4B.13),** which was attributed to the loss of moisture content. The disintegration of the cholate and zirconium network, as well as the breakdown of the cholate molecule, are responsible for about 80% of the weight loss.

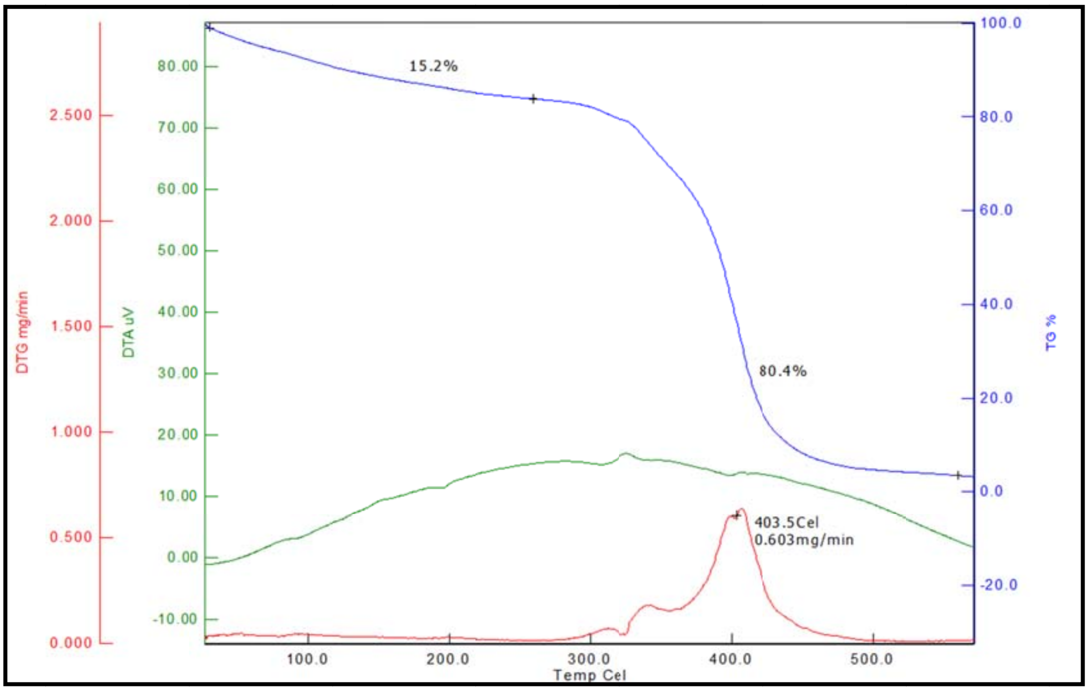

**Fig. 4B.13.** TGA spectra of Zr-CH

**4B.3.5. XPS:** XPS analysis **(Figure 4B.14)** was used to further investigate the composition of Zr-CH and Zr-CHF. Peaks in the survey spectra **(Figure 4B.14(a))** that may be attributed to the binding energies of zirconium, oxygen, carbon, and nitrogen were observed. The atomic percent of the elements were further elucidated. It was found that 31.91% was attributed to O1s, 54.47% to C1s, 9.58% to Zr3d, and 4.04% to N1s. The zirconium peak shifted towards higher binding energy after fluoride adsorption as seen in **Figure 4B.14(b and c)** showing the transfer of electrons from zirconium to fluoride. The deconvoluted spectra of F1s **(Figure 4B.14(d))** showed the presence of two peaks at 684.13 eV and 685.46 eV can be attributed to NaF and ZrF4 species.

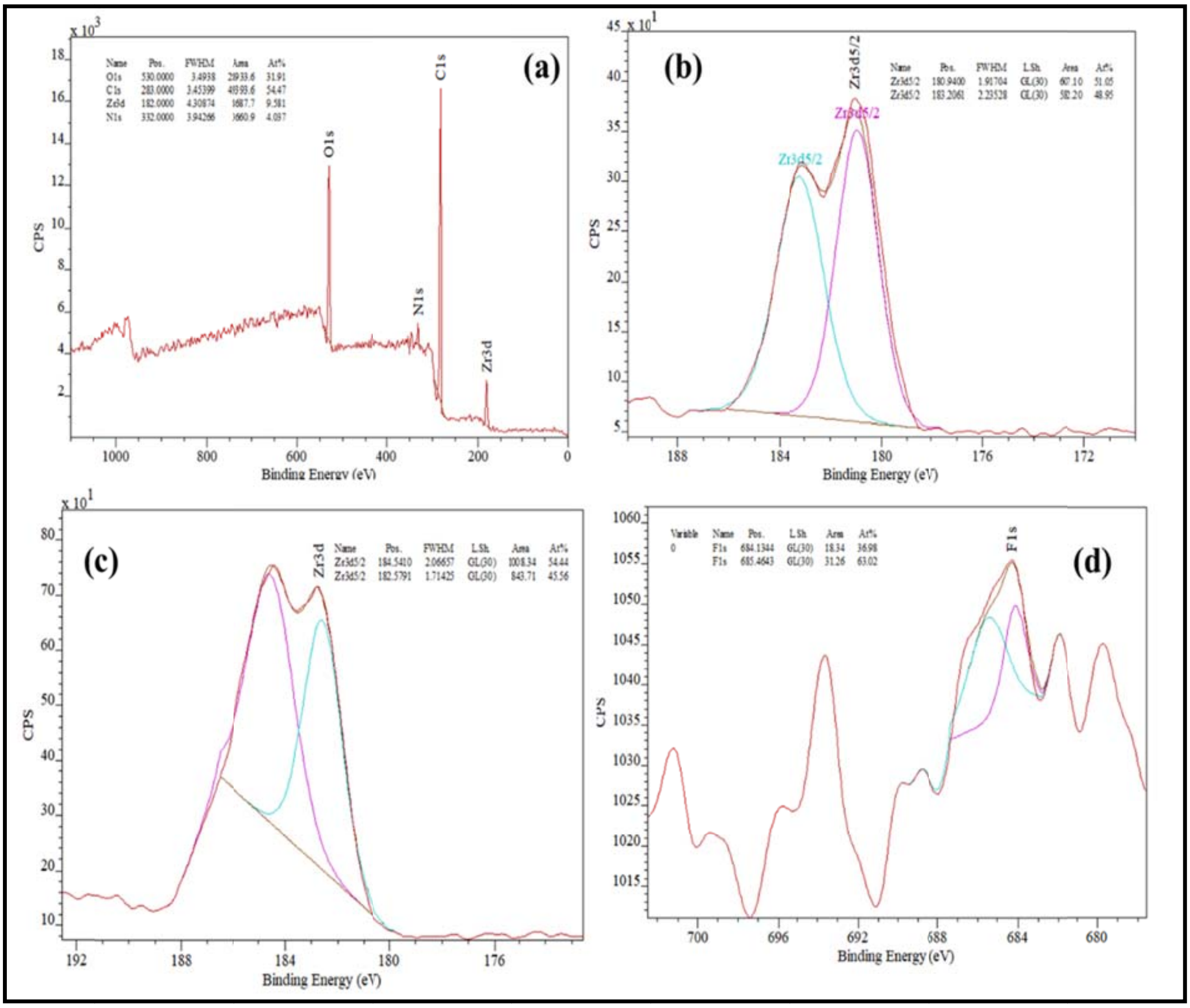

| Name | Pos. | FWHM | Area | At% |
|---|---|---|---|---|
| O1s | 530.0000 | 3.4938 | 21933.6 | 31.91 |
| C1s | 283.0000 | 3.45399 | 40993.6 | 54.47 |
| Zr3d | 182.0000 | 4.30874 | 1687.7 | 9.581 |
| N1s | 332.0000 | 3.94266 | 1660.9 | 4.037 |

| Name | Pos. | FWHM | L.Sh. | Area | At% |
|---|---|---|---|---|---|
| Zr3d5/2 | 180.9400 | 1.91704 | GL(30) | 607.10 | 51.05 |
| Zr3d5/2 | 183.2061 | 2.23528 | GL(30) | 582.20 | 48.95 |

| Name | Pos. | FWHM | L.Sh. | Area | At% |
|---|---|---|---|---|---|
| Zr3d5/2 | 184.5410 | 2.06657 | GL(30) | 1008.34 | 54.44 |
| Zr3d5/2 | 182.5791 | 1.71425 | GL(30) | 843.71 | 45.56 |

| Variable | Name | Pos. | L.Sh. | Area | At% |
|---|---|---|---|---|---|
| 0 | F1s | 684.1344 | GL(30) | 18.34 | 36.98 |
|  | F1s | 685.4643 | GL(30) | 31.26 | 63.02 |

**Fig. 4B.14.** XPS spectra **(a)** survey spectra of Zr-CH **(b)** deconvoluted spectra of zirconium of Zr-CH, **(c)** deconvoluted spectra of zirconium of Zr-CHF, and **(d)** deconvoluted spectra of fluoride of Zr-CHF

## Conclusion

In conclusion, Zr-CH has been synthesized successfully for the first time and has been characterized using XRD, XPS, TGA, EDS, SEM, and FTIR spectroscopy techniques. SEM-EDS, XRD, and XPS techniques have been used to examine the surface morphology and elemental properties of the adsorbent before and after fluoride adsorption. Langmuir isotherm and pseudo-second-order kinetic models better fit the adsorption data. Additionally, the adsorption equilibrium was reached in about 90 minutes, with maximum adsorption occurring in 30 minutes. It could be concluded that the chemisorption mechanism and monolayer adsorption of fluoride on Zr-CH were responsible for the fluoride removal. The Zr-CH adsorbent could show potential for fluoride removal, and it showed maximum adsorption ($q_{max}$=37.04mg/g) at 2 pH. Even at 7 pH, the monolayer adsorption capacity of fluoride by Zr-CH was found to be 8.40mg/g. Zr-CH has the potential to de-fluoridate water with very little interference from competing anions like bicarbonate, carbonate, nitrate chloride, and sulfate. XPS analysis of Zr-CH and Zr-CHF revealed the formation of $ZrF_4$ and NaF species. The removal mechanism may be electrostatic attraction, surface complexation, and ion exchange.

## References

Ali I, Alothman ZA, Sanagi MM. Green Synthesis of Iron Nano-Impregnated Adsorbent for Fast Removal of Fluoride from Water. Journal of Molecular Liquids 2015; 211: 457-465.

Barreca D, Gasparotto A, Maragno C, Tondello E. Nanocrystalline Lanthanum Oxyfluoride Thin Films by XPS. Surface Science Spectra 2005; 11: 52-58.

Chakraborty V, Das P. Investigation on efficiency of synthesized lanthanum oxide–coated biochar and graphene oxide–coated biochar on removal of fluoride: batch and fixed bed continuous reactor performance modelling. Biomass Conversion and Biorefinery 2022.

Chen C-L, Shih Y-J, Su JF, Chen K-L, Huang C-P. Mesoporous zirconium pyrophosphate for the adsorption of fluoride from dilute aqueous solutions. Chemical Engineering Journal 2022; 427: 132034.

Dong S, Wang Y. Characterization and adsorption properties of a lanthanum-loaded magnetic cationic hydrogel composite for fluoride removal. Water Research 2016; 88: 852-860.

Dou X, Mohan D, Pittman CU, Yang S. Remediating fluoride from water using hydrous zirconium oxide. Chemical Engineering Journal 2012; 198-199: 236-245.

El-Nemr MA, Aigbe UO, Hassaan MA, Ukhurebor KE, Ragab S, Onyancha RB, et al. The use of biochar-NH2 produced from watermelon peels as a natural adsorbent for the removal of Cu(II) ion from water. Biomass Conversion and Biorefinery 2022.

Gan Y, Wang X, Zhang L, Wu B, Zhang G, Zhang S. Coagulation removal of fluoride by zirconium tetrachloride: Performance evaluation and mechanism analysis. Chemosphere 2019; 218: 860-868.

Goswami R, Kumar M. Removal of fluoride from aqueous solution using nanoscale rice husk biochar. Groundwater for Sustainable Development 2018; 7: 446-451.

Gwardiak S, Szczęśniak B, Choma J, Jaroniec M. Benzene adsorption on synthesized and commercial metal–organic frameworks. Journal of Porous Materials 2019; 26: 775-783.

Habibi N, Rouhi P, Ramavandi B. Modification of Tamarix hispida Biochar by Lanthanum Chloride for Enhanced Fluoride Adsorption from Synthetic and Real Wastewater. Environmental Progress & Sustainable Energy 2019; 38: S298-S305.

He J, Yang Y, Wu Z, Xie C, Zhang K, Kong L, et al. Review of fluoride removal from water environment by adsorption. Journal of Environmental Chemical Engineering 2020; 8: 104516.

He Y, Zhang L, An X, Wan G, Zhu W, Luo Y. Enhanced fluoride removal from water by rare earth (La and Ce) modified alumina: Adsorption isotherms, kinetics, thermodynamics and mechanism. Science of The Total Environment 2019; 688: 184-198.

Hossien Saghi M, Chabot B, Rezania S, Sillanpää M, Akbar Mohammadi A, Shams M, et al. Water-stable zirconium and iron-based metal-organic frameworks (MOFs) as fluoride scavengers in aqueous medium. Separation and Purification Technology 2021; 270: 118645.

Jia Y, Zhu B-S, Zhang K-S, Jin Z, Sun B, Luo T, et al. Porous 2-line ferrihydrite/bayerite composites (LFBC): Fluoride removal performance and mechanism. Chemical Engineering Journal 2015; 268: 325-336.

Khan BA, Ahmad M, Iqbal S, Bolan N, Zubair S, Shafique MA, et al. Effectiveness of the engineered pinecone-derived biochar for the removal of fluoride from water. Environmental Research 2022; 212: 113540.

Kumar H, Patel M, Mohan D. Simplified batch and fixed-bed design system for efficient and sustainable fluoride removal from water using slow pyrolyzed okra stem and black gram straw biochars. ACS omega 2019a; 4: 19513-19525.

Kumar P, Prajapati AK, Dixit S, Yadav VL. Adsorption of fluoride from aqueous solution using biochar prepared from waste peanut hull. Materials Research Express 2019b; 6: 125553.

Li R, Chen B, Al-Ansari N, Aslam M, Altaf A, Elbeltagi A. Nanoarchitectonics and Kinetics Insights into Fluoride Removal from Drinking Water Using Magnetic Tea. International Journal of Environmental Research and Public Health 2022; 19: 13092.

Li W, Xie P, Zhou H, Zhao H, Yang B, Xiong J. Preparation of Lanthanum-Modified Tea Waste Biochar and Its Adsorption Performance on Fluoride in Water. Materials 2024; 17: 766.

Lingamdinne LP, Choi J-S, Angaru GKR, Karri RR, Yang J-K, Chang Y-Y, et al. Magnetic-watermelon rinds biochar for uranium-contaminated water treatment using an electromagnetic semi-batch column with removal mechanistic investigations. Chemosphere 2022; 286: 131776.

Mohan D, Kumar S, Srivastava A. Fluoride removal from ground water using magnetic and nonmagnetic corn stover biochars. Ecological Engineering 2014; 73: 798-808.

Mohan D, Sharma R, Singh V, Steele P, Pittman C. Fluoride Removal from Water using Bio-Char, a Green Waste, Low-Cost Adsorbent: Equilibrium Uptake and Sorption Dynamics Modeling. Industrial & Engineering Chemistry Research 2012; 51.

Muhammad A, Rashidi AR, Roslan A, Shah Buddin MMH. Performance Study of Watermelon Rind as Coagulants for the Wastewater Treatment. Journal of Physics: Conference Series 2020; 1535: 012053.

Pang T, Aye Chan TS, Jande YAC, Shen J. Removal of fluoride from water using activated carbon fibres modified with zirconium by a drop-coating method. Chemosphere 2020; 255: 126950.

Podgorski J, Berg M. Global analysis and prediction of fluoride in groundwater. Nature Communications 2022; 13: 4232.

Prathibha C, Biswas A, Chunduri LAA, Reddy SK, Loganathan P, Kalaruban M, et al. Zr(IV) functionalized graphene oxide anchored sand as potential and economic adsorbent for fluoride removal from water. Diamond and Related Materials 2020; 109: 108081.

Robledo-Peralta A, García-Quiñonez LV, Rodríguez-Beltrán RI, Reynoso-Cuevas L. Zr-Based Biocomposite Materials as an Alternative for Fluoride Removal, Preparation and Characteristics. Polymers 2022; 14: 1575.

Sadhu M, Bhattacharya P, Vithanage M, Padmaja Sudhakar P. Adsorptive removal of fluoride using biochar – A potential application in drinking water treatment. Separation and Purification Technology 2021; 278: 119106.

Sadhu M, P P. Lanthanum cholate fibres: A novel adsorbent for fluoride removal. Inorganic Chemistry Communications 2023; 149: 110429.

Savari A, Hamidi A, Farjadfard S, Omidvar M, Ramavandi B. Zirconium-based materials for fluoride removal from aqueous environments: A literature review and scientometric analysis. Colloid and Interface Science Communications 2023; 55: 100722.

Singh S, German M, Chaudhari S, Sengupta AK. Fluoride removal from groundwater using Zirconium Impregnated Anion Exchange Resin. Journal of Environmental Management 2020; 263: 110415.

Sonal S, Mishra BK. A comprehensive review on the synthesis and performance of different zirconium-based adsorbents for the removal of various water contaminants. Chemical Engineering Journal 2021; 424: 130509.

Tan TL, Nakajima H, Rashid SA. Adsorptive, kinetics and regeneration studies of fluoride removal from water using zirconium-based metal organic frameworks. RSC advances 2020; 10: 18740-18752.

Wang J, Chen N, Feng C, Li M. Performance and mechanism of fluoride adsorption from groundwater by lanthanum-modified pomelo peel biochar. Environmental Science and Pollution Research 2018; 25: 15326-15335.

Wang M, Yu X, Yang C, Yang X, Lin M, Guan L, et al. Removal of fluoride from aqueous solution by Mg-Al-Zr triple-metal composite. Chemical Engineering Journal 2017; 322: 246-253.

Wang Z, Shen D, Shen F, Li T. Phosphate adsorption on lanthanum loaded biochar. Chemosphere 2016; 150: 1-7.

Yan L, Gu W, Zhou N, Ye C, Yang Y. Preparation and characterization of wheat straw biochar loaded with aluminium/lanthanum hydroxides: a novel adsorbent for removing fluoride from drinking water. Environ Technol 2022; 43: 2771-2784.

Yang J-M, Hu X-W, Liu Y-X, Zhang W. Fabrication of a carbon quantum dots-immobilized zirconium-based metal-organic framework composite fluorescence sensor for highly sensitive detection of 4-nitrophenol. Microporous and Mesoporous Materials 2019; 274: 149-154.

Yang W, Shi F, Jiang W, Chen Y, Zhang K, Jian S, et al. Outstanding fluoride removal from aqueous solution by a La-based adsorbent. RSC advances 2022; 12: 30522-30528.

Yin C, Huang Q, Zhu G, Liu L, Li S, Yang X, et al. High-performance lanthanum-based metal–organic framework with ligand tuning of the microstructures for removal of fluoride from water. Journal of Colloid and Interface Science 2022; 607: 1762-1775.

Yu Y, Wang C, Guo X, Paul Chen J. Modification of carbon derived from Sargassum sp. by lanthanum for enhanced adsorption of fluoride. J Colloid Interface Sci 2015; 441: 113-20.

Zhang J, Chen N, Su P, Li M, Feng C. Fluoride removal from aqueous solution by Zirconium-Chitosan/Graphene Oxide Membrane. Reactive and Functional Polymers 2017; 114: 127-135.

Zhang J, Kong Y, Yang Y, Chen N, Feng C, Huang X, et al. Fast Capture of Fluoride by Anion-Exchange Zirconium–Graphene Hybrid Adsorbent. Langmuir 2019a; 35: 6861-6869.

Zhang T, Li Q, Xiao H, Lu H, Zhou Y. Synthesis of Li–Al Layered Double Hydroxides (LDHs) for Efficient Fluoride Removal. Industrial & Engineering Chemistry Research 2012; 51: 11490-11498.

Zhang Y, Qian Y, Li W, Gao X, Pan B. Fluoride uptake by three lanthanum based nanomaterials: Behavior and mechanism dependent upon lanthanum species. Science of The Total Environment 2019b; 683: 609-616.

Zhao W, Chen Y, Zhang W. Rapid and convenient removal of fluoride by magnetic magnesium–aluminum–lanthanum composite: Synthesis, performance and mechanism. Asia-Pacific Journal of Chemical Engineering 2017; 12: 640-650.

Zhou J, Liu Y, Han Y, Jing F, Chen J. Bone-derived biochar and magnetic biochar for effective removal of fluoride in groundwater: Effects of synthesis method and coexisting chromium. Water environment research 2019; 91: 588-597.

Zhou J, Zhu W, Yu J, Zhang H, Zhang Y, Lin X, et al. Highly selective and efficient removal of fluoride from ground water by layered Al-Zr-La Tri-metal hydroxide. Applied Surface Science 2018; 435: 920-927.

Zhou N, Guo X, Ye C, Yan L, Gu W, Wu X, et al. Enhanced fluoride removal from drinking water in wide pH range using La/Fe/Al oxides loaded rice straw biochar. Water Supply 2022; 22: 779-794.

Zhu J, Lin X, Wu P, Zhou Q, Luo X. Fluoride removal from aqueous solution by Al(III)–Zr(IV) binary oxide adsorbent. Applied Surface Science 2015; 357: 91-100.